

Observations of Atypical Rapid Intensification Characteristics in Hurricane Dorian (2019)

DAVID R. RYGLICKI,^a CHRISTOPHER S. VELDEN,^b PAUL D. REASOR,^c DANIEL HODYSS,^d AND JAMES D. DOYLE^a

^a Marine Meteorology Division, Naval Research Laboratory, Monterey, California

^b Cooperative Institute for Meteorological Satellite Studies, University of Wisconsin–Madison, Madison, Wisconsin

^c NOAA/Atlantic Oceanographic and Meteorological Laboratory/Hurricane Research Division, Miami, Florida

^d Remote Sensing Division, Naval Research Laboratory, Washington, D.C.

(Manuscript received 17 December 2020, in final form 17 March 2021)

ABSTRACT: Multiple observation and analysis datasets are used to demonstrate two key features of the atypical rapid intensification (ARI) process that occurred in Atlantic Hurricane Dorian (2019): 1) precession and nutations of the vortex tilt and 2) blocking of the impinging upper-level environmental flow by the outflow. As Dorian came under the influence of an upper-level anticyclone, traditional methods of estimating vertical wind shear all indicated relatively low values were acting on the storm; however, high-spatiotemporal-resolution atmospheric motion vectors (AMVs) indicated that the environmental flow at upper levels was actually impinging on the vortex core, resulting in a vertical tilt. We employ a novel ensemble of centers of individual swaths of dual-Doppler radar data from WP-3D aircraft to characterize the precession and wobble of the vortex tilt. This tilting and wobbling preceded a sequence of outflow surges that acted to repel the impinging environmental flow, thereby reducing the shear and permitting ARI. We then apply prior methodology on satellite imagery for distinguishing ARI features. Finally, we use the AMV dataset to experiment with different shear calculations and show that the upper-level cross-vortex flow approaches zero. We discuss the implication of these results with regard to prior works on ARI and intensification in shear.

KEYWORDS: Wind shear; Tropical cyclones; Satellite observations

1. Introduction

Major Hurricane Dorian was the strongest and most damaging tropical cyclone (TC) of the 2019 North Atlantic (NATL) hurricane season (Avila et al. 2020). Over the 14 days of its existence as a coherent, named system, Dorian directly affected: the Windward Islands, the U.S. Virgin Islands, Puerto Rico, the southeastern U.S. coast from Florida to North Carolina, and then finally the Canadian Maritimes as an extratropical system. With peak landfalling winds of 160 kt (approximately 80 m s^{-1}) on Great Abaco Island, it tied the 1935 “Labor Day” hurricane as the strongest landfalling hurricane in terms of wind speed in the Atlantic record. The reduction of steering currents and slow motion of Dorian resulted in nearly three consecutive days of at least tropical storm winds in the Bahamas. Ultimately, Dorian was responsible for \$3.4 billion in damage and the loss of 74 lives in the Bahamas alone.

According to the National Hurricane Center (NHC) report (Avila et al. 2020), track forecasts were generally good except for the short period of time when Dorian stalled over the Bahamas. While some of the numerical guidance and the official forecast did anticipate a slowdown of Dorian, they did not foresee its stalling over the Bahamas. As a result, forecasts from 28 to 30 August brought Dorian over the Florida peninsula. In terms of intensity, with the exception of the Corrected Consensus (HCCA) and the Florida State Superensemble (FSSE), Avila et al. noted: “. . . the rest of the models produced errors larger than the official forecast. Most of the large errors are related to the fact that Dorian’s center did not move over

Hispaniola, and the failure in forecasting rapid intensification when Dorian was near the Bahamas. It is important to note that none of the intensity models were [*sic*] able to capture the intensity trend of Dorian five days prior to the hurricane reaching its peak intensity of 160 kt.”

The implication of the official report is that the rapid intensification of Dorian prior to its reaching the Bahamas was largely unexpected, given the numerical guidance. Despite the fact that intensity forecasting is improving overall (Sampson et al. 2018), the accurate forecasting of rapid intensification (RI; an increase of maximum sustained surface winds of at least 30 kt or 15 m s^{-1} in 24 h) still remains a significant challenge (Knaff et al. 2020; Fischer et al. 2019; Knaff et al. 2018; Rogers et al. 2013; Krishnamurti et al. 2005). There have been several statistical–dynamical hybrid models devoted strictly to capturing RI episodes such as the Statistical Hurricane Intensity Prediction System (SHIPS) Rapid Intensification Index (SHIPS-RII; Kaplan et al. 2010), a refinement of that method incorporating passive microwave observations (Rozoff et al. 2015), and the Rapid Intensification Prediction Aid (RIPA; Knaff et al. 2018, 2020). Some of the environmental fields these techniques incorporate are deep-layer (i.e., 200 hPa minus 850 hPa) vertical wind shear, low- and/or midlevel relative humidity, upper-level divergence, and either sea surface temperature (SST) or ocean heat content (OHC). Low wind shear, high values of relative humidity, high values of upper-level divergence, and high values of the thermodynamic ocean component will all indicate increased probabilities of RI. Remote sensing observations from both geostationary and microwave satellite instruments serve as nowcasting tools to extract vortex-scale convective behavior. For example, RIPA uses the percentage of infrared (IR) pixels near the storm

Corresponding author: David R. Ryglicki, david.ryglicki@nrlmry.navy.mil

center colder than -50° and -60°C (PC50 and PC60, respectively) as a part of a simple scene analysis to quantify the vigor of convective activity (Knaff et al. 2014).

Determining convective activity has been shown to be a good indicator of intensification rate (Hazelton et al. 2017a,b; Guimond et al. 2016; Steranka et al. 1986); however, Wadler et al. (2018) and Rogers et al. (2013) demonstrated that there is nuance associated with the distribution of convection. The radius of maximum winds (RMW) usually slopes outward with height. Rogers et al. (2013) illustrated that for intensifying TCs, there exists a ring of vorticity within the RMW and convective activity for intensifying TCs is localized within this vorticity ring and within the RMW in the vertical. For steady state TCs, the vorticity profile is monopole-like in nature in the inner core and the slope of the convective activity is greater than that of the RMW. Wadler et al. (2018) expanded this to include studies of TCs in shear and demonstrated that if convective activity wraps around the core upshear, then that also indicates intensification.

Both forecasting and understanding RI in vertical wind shear present unique challenges, since shear is often thought to be overwhelmingly negative for the intensification of TCs as shear affects TCs negatively in a variety of ways (see Riemer and Laliberté 2015 and references therein). In RIPA and SHIPS-RII, shear is the predictor with the largest negative weighting; however, Knaff et al. (2020) admit that there are cases where the environmental shear parameters belie the behavior of the TC. Onderlinde and Nolan (2016) and Finocchio et al. (2016) have demonstrated that the vertical structure of the environmental winds—helical turning of the wind with height and depth and height of the layer of shear, respectively—also can affect intensification in shear. The finding that vertically shallow environmental wind profiles are more favorable for TC intensification was leveraged in a series of papers that described a new pathway to intensification in shear dubbed by the authors as “atypical RI” (Ryglicki et al. 2018a,b, 2019, 2020; hereafter Part I, Part II, Part III, and RHR). In brief, atypical RI (ARI) is characterized by the presence of tilt-modulated convective asymmetries (TCA; Part I) whereby the convection is modulated by nutations of the tilt of the vortex in shear (Part II). Stated simply, the evolution of the tilt can be divided into two separate spatial and temporal scales: the longer, larger precession and shorter, smaller nutations (Part II). A nutation is a smaller-scale, higher-frequency wobble superposed on the larger and slower precession. The precession is the change in the orientation of the rotational axis of the vortex (Jones 1995; Reasor et al. 2004; Schecter 2015; Reasor and Montgomery 2015). TCAs are convective phenomena distinct from the larger diurnal signal (Kossin 2002; Dunion et al. 2014) and smaller-scale convective bursts (Guimond et al. 2010) and exist on top of the central dense overcast (CDO). For example in Part II, nutations were responsible for repeated 15-km tilt oscillations over the span of 9 h, while the larger tilt associated with the precession decreased from 55 to 0 km over the span of 3.5 days. When the nutation magnitudes and the precession magnitude became coincident, TCAs appeared. A key feature of the TCAs is that the outflow associated with them reroutes the environmental

flow around the TC thus reducing the shear and permitting realignment, but this blocking is only effective if the environmental wind forcing is vertically shallow (Part III). What separates this outflow from outflow in a more classical, nonsheared TC is that this outflow is strongly divergent, and it is the divergent component of the flow which is responsible for the blocking effects (RHR).

At first glance, the application of ARI concepts to Dorian would seem misguided, since the NHC report does not make mention of moderate- to high-shear values either during or directly preceding Dorian’s RI, with the reminder that moderate shear is a necessary requirement for ARI as it forces the tilt. In the NHC report of 2016 NATL Matthew, for example (Stewart 2017; Part III), the mischaracterization of shear is prominently mentioned as a potential reason for the RI forecasting discrepancy. Since the numerical guidance largely missed Dorian’s RI event, we focus on observations of the storm from two data sources: WP-3D dual-Doppler radar and GOES-16 high-spatiotemporal-resolution atmospheric motion vectors (AMVs). Using novel analytical methods, we investigate the structure of the vortex both internally and aloft, focusing on the evolution of the tilt and the storm-top outflow. Section 2 describes the data and the methodologies used to process the data. Section 3 reviews the track and forecasting history of Dorian and then presents the findings from the analysis of the AMV and WP-3D radar datasets. Section 4 applies existing ARI methods to more deeply investigate the shear evolution. Section 5 summarizes and discusses the findings herein.

2. Data and methods

a. General data information

Multiple datasets are used to analyze Dorian’s evolution. Dorian existed from 24 August to 7 September, but we focus on the rapid intensification period spanning 0000 UTC 30 August to 1200 UTC 1 September. We use a combination of GFS analyses, GOES-16 “clean” IR (channel 13, $10.3\text{ }\mu\text{m}$) brightness temperature imagery, airborne dual-Doppler radar data from the Hurricane Research Division (HRD) archives, a postprocessed GOES-16 AMV dataset and derived shear products provided by the Cooperative Institute for Meteorological Satellite Studies (CIMSS) at the University of Wisconsin, the best track archive (HURDAT; Landsea and Franklin 2013), the SHIPS data archive (DeMaria et al. 2005), and the model forecast archive from the Automated Tropical Cyclone Forecasting system (ATCF; Sampson and Schrader 2000). The GFS analyses are converted into rotational and divergent winds using SPHEREPACK (Adams and Swartztrauber 1997). The dual-Doppler radar data comes from both WP-3D Orion aircraft, NOAA42 and NOAA43, in its postprocessed state where it exists on a regular grid with 2-km grid spacing in the horizontal and 500-m spacing in the vertical out to 250 km from the TC center (Reasor et al. 2013). We temporally constrain our analyses based on the availability of the unique AMV dataset. Normally, AMVs are produced hourly and are used most often in 3-h intervals.

b. AMV processing

For this study, AMV datasets were reprocessed by CIMSS from *GOES-16* Advanced Baseline Imager (ABI) rapid scan imagery for the duration of Dorian when the “meso sector” was targeting the TC. This occurred from 0000 UTC 30 August to 1200 UTC 1 September, fully encompassing Dorian’s unexpected RI. The imagery is available at 1-min intervals. Special processing strategies were imposed to enhance AMV coverage and maximize the information content to resolve the scales of the flow fields associated with the storm vortex and its near environment; current operational AMV retrieval methods would not be sufficient for the analyses to follow. This methodology results in an AMV dataset whose observational period is 15 min for the duration of the 60 h that the meso sector was used to monitor Dorian. The derived AMVs are then grouped into three layers: surface to 650 hPa, 650 to 250 hPa, and 250 hPa and higher. The layers are then resampled to a storm-relative cylindrical grid, emphasizing the broadscale features of the flow in which we are most interested. For more information on the data retrieval procedures and the resampling methodology, see [appendix A](#).

c. WP-3D radar data processing

Multiple prior studies have used airborne radar data for various TC-related analyses ([Zawislak et al. 2016](#); [Reasor et al. 2013](#); [Rogers et al. 2013](#); [Stevenson et al. 2014](#)), but when analyzing the structure and, in particular, the tilt of TCs from observations, prior studies have usually used composites of two or more swaths (i.e., radial passes through the TC center) from a given flight. Since we seek to characterize tilt variability on shorter time scales (see [section 3b](#)), we calculate the tilt from individual swaths. A significant drawback of attempting to compute structural diagnostics like vortex tilt from individual swaths is data availability. The data are limited to 50 km from the flight track and subject to the precipitation distribution, variations in beam geometry, signal attenuation, and QC constraints. We thus use an ensemble of centers and various interpolation techniques to judge confidence of the center position. Details on the ensemble methodology can be found in [appendix B](#).

To quantify the uncertainty of the center, we calculate normalized spread, as defined similarly to [Rygllicki and Hodyss \(2016\)](#):

$$s(z) = \frac{\sqrt{\frac{1}{M} \sum_{m=1}^M [\Delta_m(z)]^2}}{\text{RMW}(z)}, \quad (1)$$

where s is the normalized spread, z is the vertical level, M is the number of center-finding methods (nine, see [appendix B](#)), m is a given method, Δ_m is the Euclidean distance between a calculated center and the mean of the centers for a given height, and RMW is the average radius of maximum winds of the methods for a given height. [Figure 1](#) is the visualization of this quantity for the relevant flights and shows an example where the spread is high ([Fig. 1a](#)) and where it is low ([Fig. 1b](#)). Generally speaking, if a swath captures both sides of a distinct eyewall during a flight, then the methods will be in agreement

([Figs. 1b,c](#)). We use the value of 0.1 as a cutoff for high confidence since that is the ratio at which the aliasing of the mean tangential wind onto the wavenumber-1 radial wind is within the noise of the signal ([Rygllicki and Hodyss 2016](#)), although other small values are still useful. In physical space, since the low-level RMW of Dorian is usually at or below 20 km (see [section 3](#)), a normalized spread of 0.1 is approximately 2 km for this case. It is important to keep in mind that the spread in physical space will increase with height due to the outward slope of the TC eyewall and also since the TC becomes less well defined at higher levels in the troposphere ([Shea and Gray 1973](#)). Our analyses occur at times and levels when the spread is small; therefore, we are confident in our tilt analyses later in the manuscript. As a final note, the low-level center is defined as the average center position of the mean centers from 0.5-, 1.0-, and 1.5-km heights.

d. GOES-16 IR image processing

As in [Part I](#), a windowed-sinc filter ([Smith 2003](#)) is used in low-pass and bandpass modes on total cloud coverage colder than -70°C in a 200-km circle centered on the best track location. The difference here is that while [Part I](#) used a Blackman–Nuttall window ([Nuttall 1981](#)), we employ a more customizable Kaiser window with an attenuation of 40 dB ([Kaiser and Schafer 1980](#)). The full expression of the filter is

$$F(t) = f(t) * \text{sinc} \left[2f_c \left(n - \frac{N-1}{2} \right) \right] \times \left[\frac{I_0 \left(\beta \sqrt{1 - \left(\frac{2n}{N-1} - 1 \right)^2} \right)}{I_0(\beta)} \right], \quad (2)$$

where F is the transformed signal, f is the original signal, t is the time, the asterisk is shorthand for the “convolve” operation, f_c is the cutoff frequency, n is the index of a given observation in the time series, N is the length of the window, I_0 is a Bessel function of the first kind, and β is a derived parameter related to the roll-off and the attenuation ([Kaiser and Schafer 1980](#)). Edges are zero-padded. Since we use the filter to remove any diurnal signal, the cutoff frequency is equivalent to 18 h with a roll-off of approximately the equivalent of 4 h on either side of the cutoff frequency. After the diurnal signal has been removed, a continuous wavelet transform is employed to determine temporal patterns in the resultant signal. Similar to [Part I](#), the wavelet used is the Morlet and has the following form:

$$\Psi_0(t) = \pi^{-1/4} e^{i\omega_0 t} e^{-t^2/2}, \quad (3)$$

which is a plane wave multiplied by a Gaussian.

3. Synoptic overview, AMV analyses, and radar analyses

a. Synoptic and forecasting overview

Dorian’s origins can be traced to a tropical wave that exited the West African coast on 19 August. The wave began showing

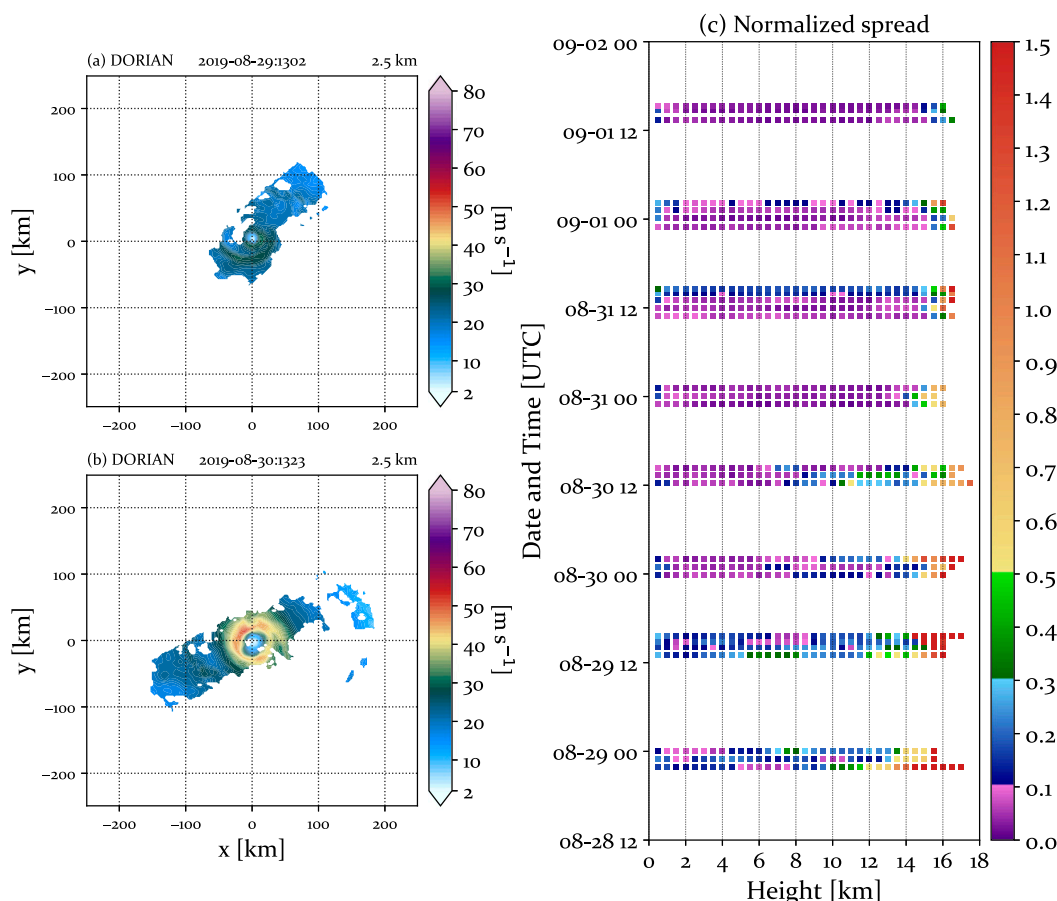


FIG. 1. Two examples of wind swaths at 2.5-km altitude indicating swaths resulting in (a) low center-finding confidence and (b) high center-finding confidence. (c) The normalized spread (see text for definition) at each available level for each of the swaths between 1200 UTC 28 Aug and 0000 UTC 2 Sep. The times of the two examples are (a) 1302 UTC 29 Aug and (b) 1323 UTC 30 Aug.

signs of organization on 22 August, and it was finally categorized a depression at 0600 UTC 24 August. Figure 2 illustrates the evolution and track of Dorian as it intensified past the Windward Islands and moved north of Puerto Rico, becoming a hurricane. Dorian then proceeded to rapidly intensify over the following two days. It reached the Bahamas on 1 September, stalled for three days, and was eventually swept to the north by a midlatitude trough. It brushed the coasts of Florida, Georgia, South Carolina, and North Carolina before finally making landfall as an extratropically transitioning system in the Canadian Maritimes (Avila et al. 2020). We focus on the time period after it passed Puerto Rico and before it reached the Bahamas, indicated by the black crosses in Fig. 2.

Figure 3 shows select fields drawn from the operational SHIPS database plus the AMV-derived CIMSS shear. Early on in Dorian's development, the shear was low, between 1 and 5 m s^{-1} (Fig. 3a), well within the climatological RI range of the Atlantic (Kaplan et al. 2010). Depending on the particular shear-calculating method, Dorian continued to intensify in shear ranging from 3 to 8 m s^{-1} . After intensification stalled on 29 August as a category-1 hurricane, Dorian rapidly intensified

over the next 3 days to a category-5 hurricane, eventually surpassing its maximum potential intensity (MPI) on 1 September. In terms of the moist thermodynamics, SSTs underneath Dorian were consistently above 28°C for practically its entire existence. The humidity values (Fig. 3b) were relatively low for the first third of its existence. In a quantitative sense, using SHIPS-RII climatology (Kaplan et al. 2010), the average RHLO value for TCs undergoing RI is 73.5% with a standard deviation of 6.2%. The RHLO values were below one standard deviation (67.3%) for nearly the first 5 days of its existence.

With regard to intensity forecasts, Fig. 4 accumulates forecasts on 30 and 31 August from a variety of dynamical and statistical models. With the exception of early forecast lead times from HMON, all of the models missed Dorian's maximum intensity. Despite missing the peak intensity, HMON was perhaps the only model to at least hint at the rate of intensification early in its forecasts. The intensity forecasts level off with increasing initialization time, with most intensification nearly arrested completely at 1200 UTC 30 August (Fig. 4d). Given the consistent signal in all of the models, it would indeed seem as if this RI was unexpected.

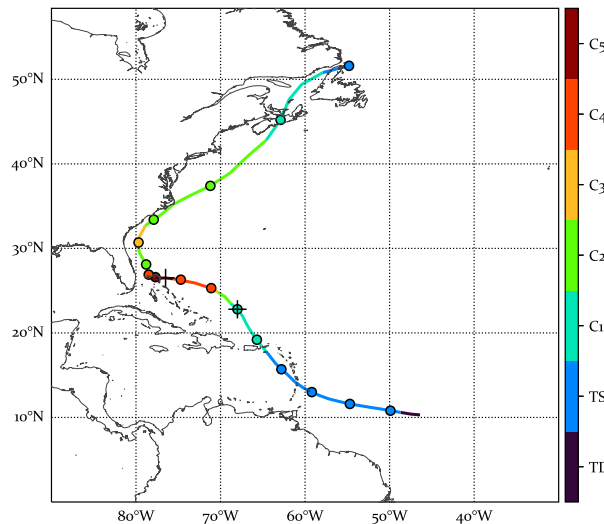


FIG. 2. Track of Hurricane Dorian, color-coded by Saffir-Simpson intensity. Dots are 0000 UTC for each day. Black crosses indicate start (0000 UTC 30 Aug) and end (1200 UTC 1 Sep) of AMV special observing period.

Despite the fact that model forecasts are generally poor at capturing the full ARI behavior, there is still utility in inspecting global model analysis and reanalysis fields (Part III, RHR). At upper levels, divergent winds acts to reroute the environmental flow. At analysis time, both GFS analyses (Part III) and ERA5 (RHR) have been shown to provide clues that ARI might be occurring. Where shear calculations usually fail in identifying outflow blocking is either by removing the divergent component of the outflow or by using an annulus that is too large. In an attempt to provide more operational utility to this study, we use the GFS analyses. For ARI to proceed, the strongest environmental winds shearing the TC must be vertically limited to the same levels as the outflow layer in order to maximize the outflow blocking effect. Usually, but not always, this requires that the environmental shear forcing be caused by an upper-level anticyclone (Part I). As a simple analysis, we inspect 200-hPa winds from the GFS decomposed into their rotational and divergent components. Figure 5 shows the progression of the upper-level flow field in 12-h increments from 0000 UTC 29 August to 1200 UTC 31 August. At upper levels, Dorian was being sheared by an upper-level anticyclone. The GFS analyses also indicate a divergent-wind maximum on the southern side of the storm as it moves away from Puerto Rico (Figs. 5b–e), indicative of the GFS analysis’s interpretation of outflow blocking (Part III, RHR).

b. AMVs and WP-3D radar data

Despite the fact that the analyzed shear is relatively low during RI (Fig. 3), the upper-level GFS analyses do hint that outflow blocking may be taking place. We can interrogate this directly from observations using the AMVs. Figure 6 shows the evolution of the upper-layer flow as depicted by the AMVs. In Fig. 6a, the southerly upper-level environmental winds are impinging on the core of Dorian at 0115 UTC 30 August, as the

zero radial wind line south of the storm center is less than 100 km away. Then, 6 h later at 0700 UTC 30 August (Fig. 6b), it is pushed out to 150 km and subsequently much farther out at 1145 UTC (Fig. 6c). It then retreats to 100 km at 1515 UTC (Fig. 6d) before finally being pushed out again and kept away at 0300 UTC 31 August (Fig. 6e). While all of the following times during the special observing period fluctuate in the location of the zero radial wind line, Dorian has established outflow in all directions after the final pushback (Figs. 6f–i).

Outflow pushback, exemplified by the outward movement of the zero radial wind line in Fig. 6, and subsequent shear reduction (to be explored further in section 4b) over the core region is one of the major components of ARI. The other major aspect of ARI is the evolution of the tilt of the vortex. Normally, the tilt of the vortex must be abstracted from movements of the cloud shield in IR (Part I, Part II, RHR). As was shown in section 2c, Dorian was well sampled by the NOAA WP-3D aircraft, allowing for direct measurement of the tilt. Additionally, given the center-location spread analyses (Fig. 1c), we are confident in all following tilt analyses for the special observing period.

Given the evolution of the upper-level wind field (Fig. 6), we focus on the three WP-3D missions that took place on 30 August. Figure 7 displays the mean tilt evolution for three radar swaths from each of the three flights. Broadly speaking, the WP-3D observations captured the following sequence: tilt precession (Figs. 7a–c), tilt nutation (Figs. 7d–f), and full alignment (Figs. 7g–i). The observations have captured all three stages of tilt evolution of ARI (Part II). For the precession (Figs. 7a–c), a small nutation may actually be embedded within, although it is difficult to claim that definitively with only three observations spaced an hour apart. Nevertheless, both the 7- and 10-km tilt magnitudes increase during the flight early on 30 August. For the nutation portion of the evolution (Figs. 7d–f), it is clear that the highest center analyzed here, 10 km, undergoes a significant counterclockwise swing from 20 km away to the north of the low-level center, to 15 km away due northwest, and then finally 5 km again due north in only 2 h. During this time frame, the 7-km tilt migrates from 2 to 4 to 10 km radially. Finally, during the final flight on 30 August (Figs. 7g–i), Dorian is nearly fully aligned in the vertical. To compare the differing speeds of the 10-km center during the precession and nutation phases, the 10-km center moves with a speed of approximately 0.6 m s^{-1} during the precession and approximately 3.1 m s^{-1} during the nutation, respectively.

Combining the AMV dataset with the WP-3D dataset and the operational shear calculations, Fig. 8 displays the evolution of Dorian in time. The outflow and zero radial wind line, indicating the farthest extent of the outflow (Fig. 8a), is smoothed with a 1-h running mean. One of the WP-3D flights lines up during the minimum in outflow, as the wobble precedes the outflow surge starting at 1300 UTC 30 August (Fig. 8d), matching modeling studies of this phenomenon (Part III). A period of rapid intensification also occurs between 1200 UTC 30 August and 0000 UTC 31 August, as the MMTW evolution is corroborated by the best track (Fig. 8b). Interestingly, the RMW increases to 22.5 km at 1200 UTC 30 August during the nutation before essentially settling at 17 km at 0000 UTC

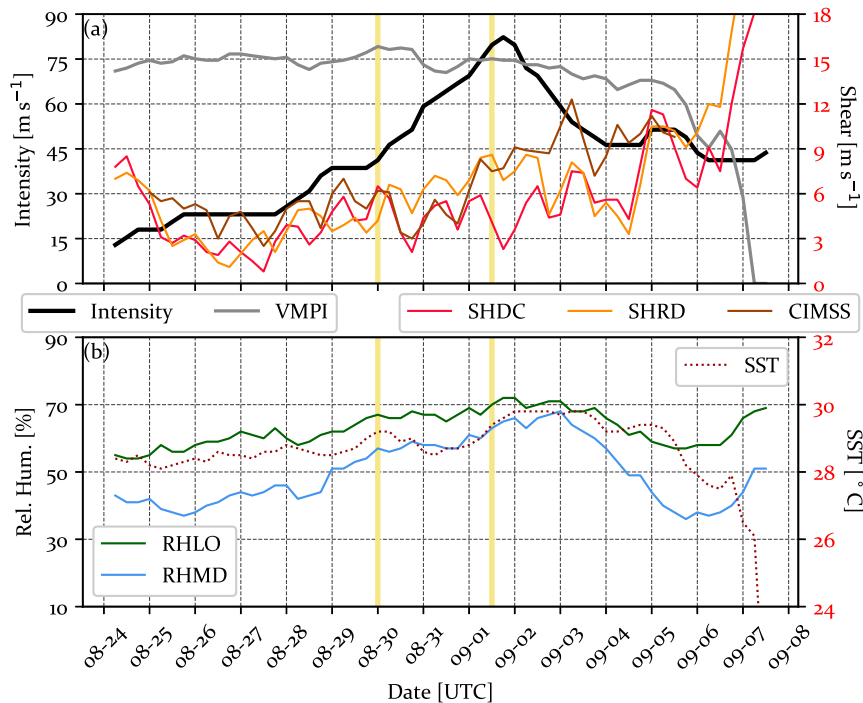


FIG. 3. (a) Intensity, MPI evolution (VMPI), and three shear calculations [SHDC (defined as 850–200-hPa shear magnitude vs time of a 500-km storm-centered circle after removing the divergent component of the wind), SHRD (defined similarly to SHDC except using an annulus of 200–800 km and no removal of the divergent component of the wind) from SHIPS, and CIMSS] during Dorian's evolution. (b) Low- and midlevel relative humidity (RHLO, RHMD) as well as sea surface temperatures (SST) during Dorian's evolution. Vertical yellow lines span the special observing period.

31 August (Fig. 8c). The TC also stays aligned beginning at 0000 UTC 31 August for the duration of the special observing period. Finally, the shear calculations reach their minima at the same time as the 1800 UTC 30 August outflow surge, but they then increase throughout the period amidst a diurnal cycle (Fig. 8e). The tilt appears to be largely unaffected by this calculated shear increase.

RHR demonstrated that the pushing effect by the outflow is related to the presence of strong updrafts in sheared TCs. Using the radar data, we can compute the distribution of updrafts for each flight swath. Figure 9 shows the updraft distribution during the precession (Figs. 9a–c), during a nutation (Figs. 9d–f), and finally at the alignment stage (Figs. 9g–i) by using log-scale contour frequency by altitude diagrams (CFADs; Yuter and Houze 1995) of all observations within 50 km of the low-level center. CFADs are useful because they clearly describe the updraft distribution and allow us to compare the updraft distribution from swath to swath. While the variability is not as dramatic as was shown in RHR, possibly due to the fact that updraft retrievals are constrained by the incompressible continuity equation and further smoothing (Gamache et al. 1994), we do see that the updraft velocities during the nutation peak at values near 10 m s^{-1} between 9 and 14 km in height just prior to the outflow pushback (Figs. 9d–f). After alignment, the CFAD distributions narrow, with the

last swath's CFAD indicating no updrafts greater than 6 m s^{-1} (Fig. 9i).

From a spatial perspective, we focus on only the most intense updrafts since they have been related to modulation of the outflow required for blocking (RHR). Figure 10 presents the winds at 2 km during each swath as well as the locations of updrafts 7 m s^{-1} or greater. While prevailing thought is that intense convective towers are related to the shear direction (e.g., Corbosiero and Molinari 2003), Part II indicated that it is the tilt orientation that is most responsible for controlling the convective activity in this situation. While there is evidence of the expected behavior of the strongest convective activity down-tilt or left of down-tilt (Figs. 10c–e), there are also examples of strong updrafts on the up-tilt side of the core (Figs. 10b,f). The evolution during the nutation (Figs. 10d–f) can be directly compared to results from Part II (their Figs. 11 and 12) as reductions in tilt are associated with the permissibility of strong convective cells on all sides of the TC core. While the 10-km center is farthest north of the low-level center, the strongest updrafts are down-tilt or left of down-tilt (Figs. 10d,e). During the relative minimum of the upper-level tilt, strong updrafts are on the up-tilt side (Fig. 10f). By the time of the full alignment (Figs. 10g–i), as confirmed by the CFADs (Figs. 9g–i), the strongest updrafts have essentially ceased.

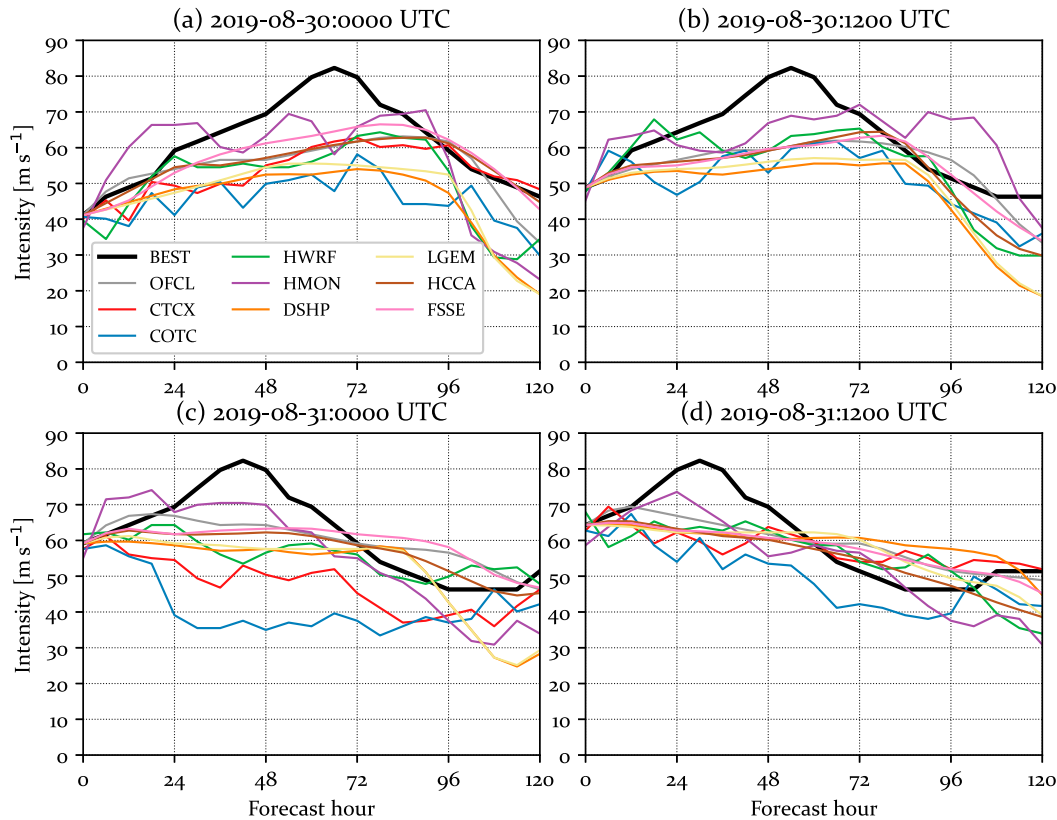


FIG. 4. Intensity forecasts of Hurricane Dorian at 0000 and 1200 UTC on two days (30 and 31 Aug) from a select group of models. See Table 1 for abbreviations.

4. Atypical rapid intensification indicators

a. Satellite-based IR image analyses

Since all of the prior observation-based ARI studies needed to abstract some of the aforementioned concepts from IR satellite imagery, we will apply those techniques to Dorian. We focus on the quantification of subdiurnal, superconvective signatures using the methods described in section 2d (Part I). We will also use the AMV data to analyze the evolution of the shear, being cognizant of the tradeoffs related to removing components of the TC outflow and circulation when calculating shear (Part III, RHR). As a first analysis, Fig. 11 shows the evolution of the cloud shield of Dorian from 1800 UTC 29 August until the eye fully appears at 0030 UTC 31 August. The coldest cloud tops barely reach out to 75 km from center on the southern side of Dorian initially (Fig. 11a). As Dorian continues to mature, the -60°C clouds begin to push farther to the south (Figs. 11c–e), agreeing with the upper-level AMV radial wind analyses in the prior section. Eventually, the expansion grows to 150 km (Fig. 11g) prior to the appearance of a distinct eye (Fig. 11h).

As in Part I, we focus on the total area covered by IR T_B colder than -70°C within 200 km of the center for our time series analyses. We then filter the time series using Eq. (2) to remove the diurnal signal and then use Eq. (3) to highlight localized packets of activity. Figure 12 displays both of these

analyses for the entirety of Dorian’s existence. Focusing on the time series first (Fig. 12a), a diurnal signal is prominent from 25 August up to and including 28 August. A notable rise in cold cloud coverage that is associated with the diurnal signal appears again on 30 August, but a smaller magnitude oscillation appears to be present within. A distinct eye subsequently appears on 31 August. As Dorian becomes a category-5 hurricane on 1 and 2 September, the cold cloud tops reach their largest

TABLE 1. Descriptions of the legend in Fig. 4.

Abbreviation	Description
BEST	Best track
OFCL	Official NHC forecast
CTCX	Coupled Ocean–Atmosphere Mesoscale Prediction System, TC version
COTC	(COAMPS-TC) with GFS boundaries
HWRF	COAMPS-TC with NAVGEM boundaries
HMON	Hurricane Weather Research and Forecasting Model
DSHP	Hurricanes in a Multiscale Ocean-coupled Nonhydrostatic model
LGEM	Decay SHIPS
HCCA	Logistic Growth Equation Model
FSSE	Corrected Consensus
	Florida State Superensemble

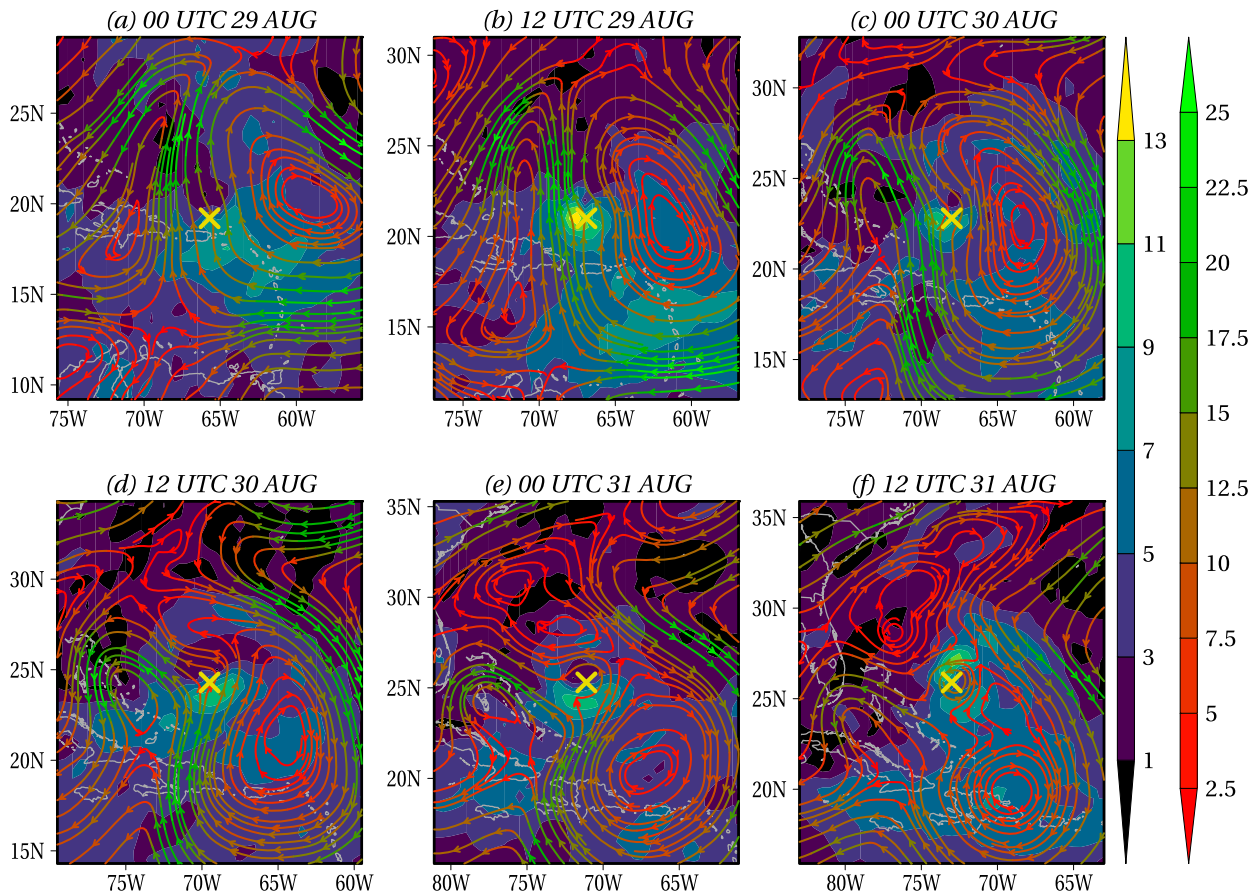


FIG. 5. GFS analyses of 200-hPa divergent (shading) and rotational (streamlines) winds (m s^{-1}) surrounding Hurricane Dorian (yellow \times) at 0000 and 1200 UTC on three days: (a),(b) 29 Aug; (c),(d) 30 Aug; and (e),(f) 31 Aug.

extent. They peak again on 5 September, but Dorian had already moved northward out of the tropics at this time. The wavelet analyses (Fig. 12b) indicate that on 30 August, the most prominent subdiurnal oscillation is between 6 and 7 h. If we continue with the assumption that the evolution of the tilt is driving the convective behavior at this time (Part I, Part II, RHR), then we hypothesize that Dorian's nutations are oscillating with a period of between 6 and 7 h on 30 August prior to the appearance of a distinct eye. Analyses of the semidiurnal signal after the eye has appeared are beyond the scope of this study.

b. AMV-derived shear calculations

A major finding of Part III and RHR was that frequently used shear calculations can mischaracterize the effective shear on a TC in two ways: by using a storm-centered averaging circle/annulus that is too large and/or by removing some or all of the outflow. For example, the SHDC method from the operational SHIPS method uses a 500-km circle but removes the divergent component of the wind, while the SHRD method uses an annulus from 200 to 800 km surrounding the TC. RHR concretely demonstrated that the divergent outflow is directly responsible for the outflow blocking phenomenon. For the forthcoming analyses, we use the upper and lower AMV layers

as described in section 2b and in appendix A. Shear is calculated thusly: zonal and meridional winds are averaged independently in a layer, and then a mean vector is computed for that layer. The shear is the difference of the mean vectors between the upper layer and the lower layer. We use three circular shapes of varying radial widths (Part III) for the upper layer: 0–200, 0–500, and 200–500 km. We use a 100–500-km annulus in the lower layer. The reason we ignore the innermost 100 km in the lower layer is that there are a few observation periods where one AMV is analyzed in or near the core, and this contaminates the lower-layer signal. We also use storm motion as an experimental alternate source of the lower component of the shear calculation. The storm motion is our attempt at corroborating and framing the lower-layer AMV-derived flow. AMV-derived calculations are smoothed with a 1-h running mean.

Figure 13 shows the shear decomposed into the lower part (Fig. 13a), the upper part (Fig. 13b), and the magnitude of the vector difference (Fig. 13c). Dorian's forward speed slows down from 4 to 2 m s^{-1} during the observing period. The lower-layer calculation tracks this reasonably well with exception of one period from 1200 to 2200 UTC 30 August, where the flow calculation is 50%–100% larger than the motion (Fig. 13a). Perhaps more important is the evolution of the upper layer.

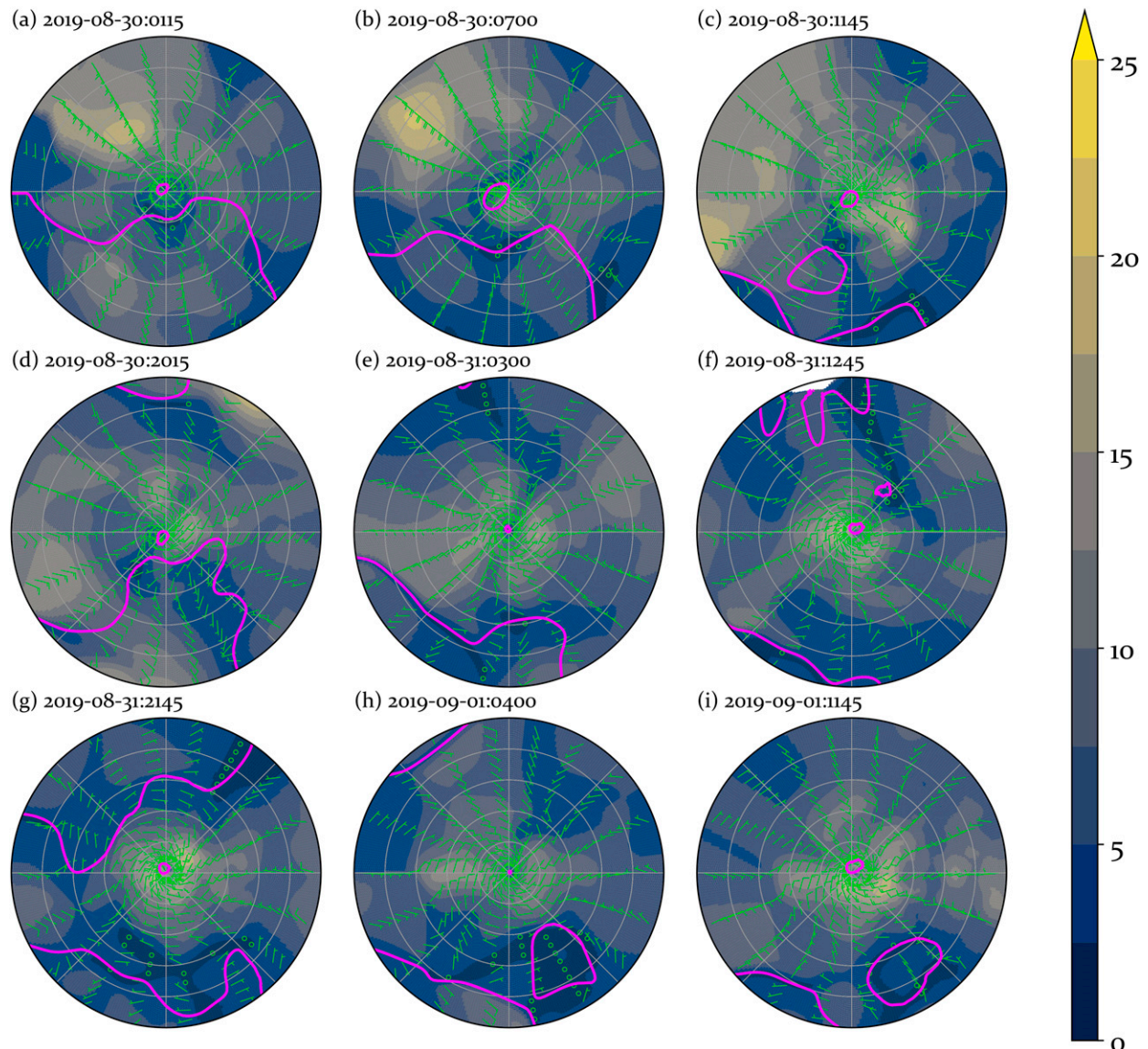


FIG. 6. Upper-layer interpolated AMV wind speed magnitudes (m s^{-1} ; shading and barbs) at (a) 0115, (b) 0700, (c) 1145, and (d) 2015 UTC 30 Aug; (e) 0300, (f) 1245, and (g) 2145 UTC 31 Aug; and (h) 0400 and (i) 1145 UTC 1 Sep. Magenta line is the zero radial wind line. Radial extent is 500 km.

The upper-layer cross-vortex flow is analyzed near 7 m s^{-1} at the start of the observing period. In the midst of the first outflow surge beginning around 0900 UTC 30 August, the flow in the smallest circle drops to 1 m s^{-1} . The two larger circles/annuli do not analyze the drop in the flow to this extent, but the three calculations converge at 1800 UTC 30 August and they essentially remain below 2 m s^{-1} for the duration of the period. When comparing all of the possible shear pairings with the traditional methods (Fig. 13c), the three operational calculations broadly capture the oscillations of the flow, although the shear combinations using the upper-layer flow and storm motion are consistently lower than the traditional calculations. If one uses the AMV-derived lower-layer flow, then this shear value does indicate short-lived shear values higher than the

operational calculations. We discuss this interesting behavior more in section 5b.

5. Summary and discussion

a. Summary

North Atlantic Major Hurricane Dorian was the most destructive TC from the 2019 season, as it ravaged the Bahamas for 3 days. Prior to its rapid intensification (RI) to a Saffir–Simpson category-5 major hurricane, the numerical guidance did not indicate that its continued intensification was likely. Given recent advancements in an alternative, shear-induced pathway to RI, previously dubbed atypical RI (ARI), we applied techniques developed to characterize this pathway (Part I,

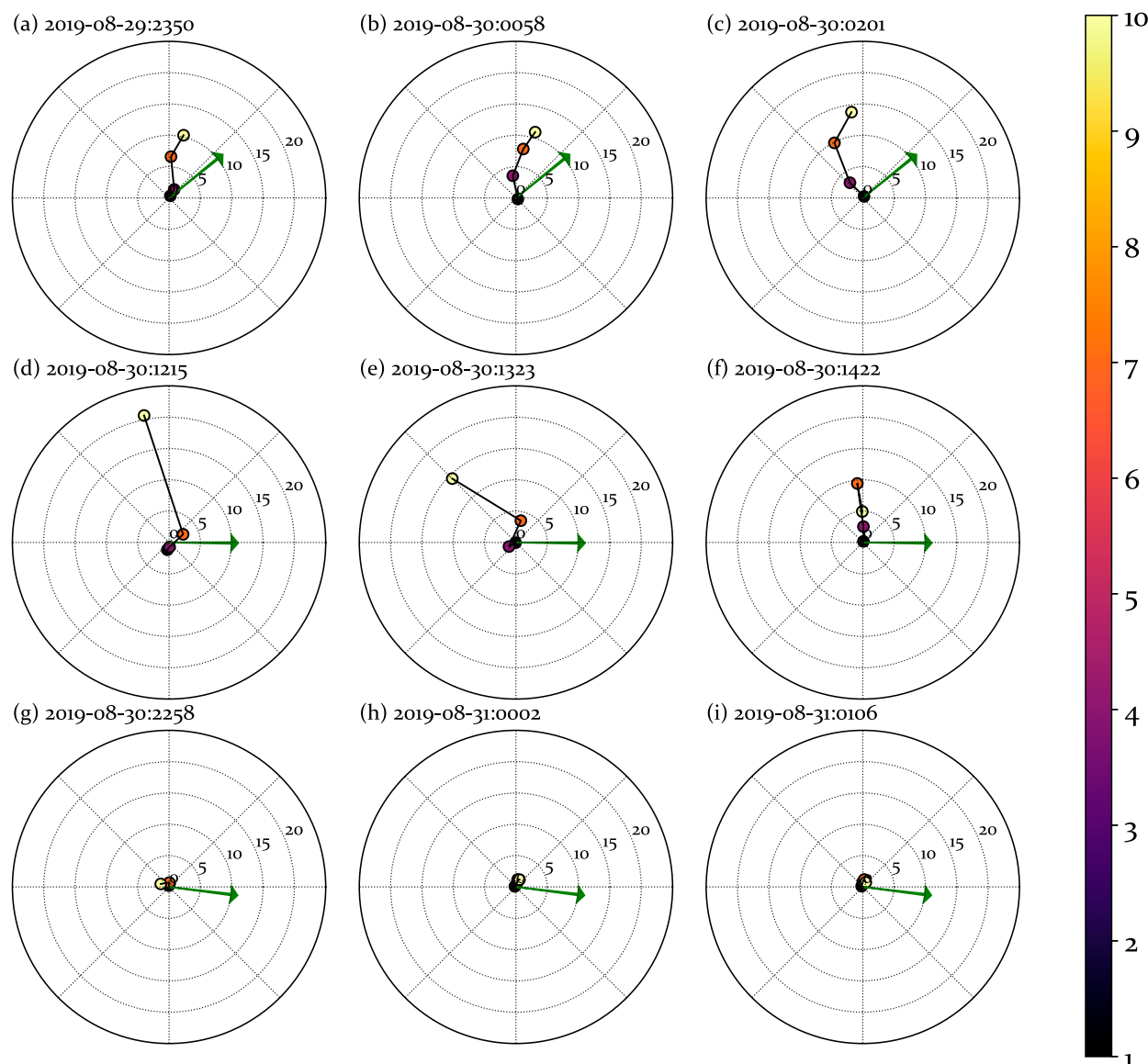


FIG. 7. Plots of the 1.0-, 4.0-, 7.0-, and 10.0-km mean centers (colored circles) for individual swaths in Dorian. The low-level center is the average of the 0.5-, 1.0-, and 1.5-km mean centers. The swath times are (a) 2350 UTC 29 Aug; (b) 0058, (c) 0201, (d) 1215, (e) 1323, (f) 1422, and (g) 2258 UTC 30 Aug; and (h) 0002 and (i) 0106 UTC 31 Aug. Green arrows are shear direction *only* as averaged from SHDC, SHRD, and CIMSS methods from the closest synoptic time. Radial units are km.

Part II, Part III, RHR) to Dorian's observations. Using a special dataset of high-spatiotemporal-resolution AMVs from *GOES-16* and serendipitous WP-3D flight observations, we demonstrated how Dorian went through the ARI process. ARI is characterized by the presence of vortex tilt nutations which modulate inner-core convection and subsequently produce outflow that blocks the environmental flow, reduces the vertical wind shear, and permits vertical realignment.

Treating the outflow layer as a slab and interpreting all of the AMVs above 250 hPa as being within this layer, we demonstrated how the environmental flow originating from an upper-level anticyclone impinged on Dorian's core. The outflow front, otherwise known as the radial wind zero line, oscillates

between 100 and 250 km upwind over the span of a day on 30 August before being pushed out permanently early on 31 August. We then showed that concurrent to the outflow behavior, radar analyses showed three distinct phases of vortex tilt: precession, nutation, and alignment. These are the three tilt phases described in previous ARI studies using an idealized full physics model (Part II). Using the area coverage of brightness temperatures below -70°C over Dorian, a wavelet analysis indicates that the subdiurnal oscillations in the cloud field occur with a period of between 6 and 7 h prior to the appearance of the eye on 31 August. If we assume that this oscillation is also associated with the nutation (Part II), then the nutation period may also be between 6 and 7 h.

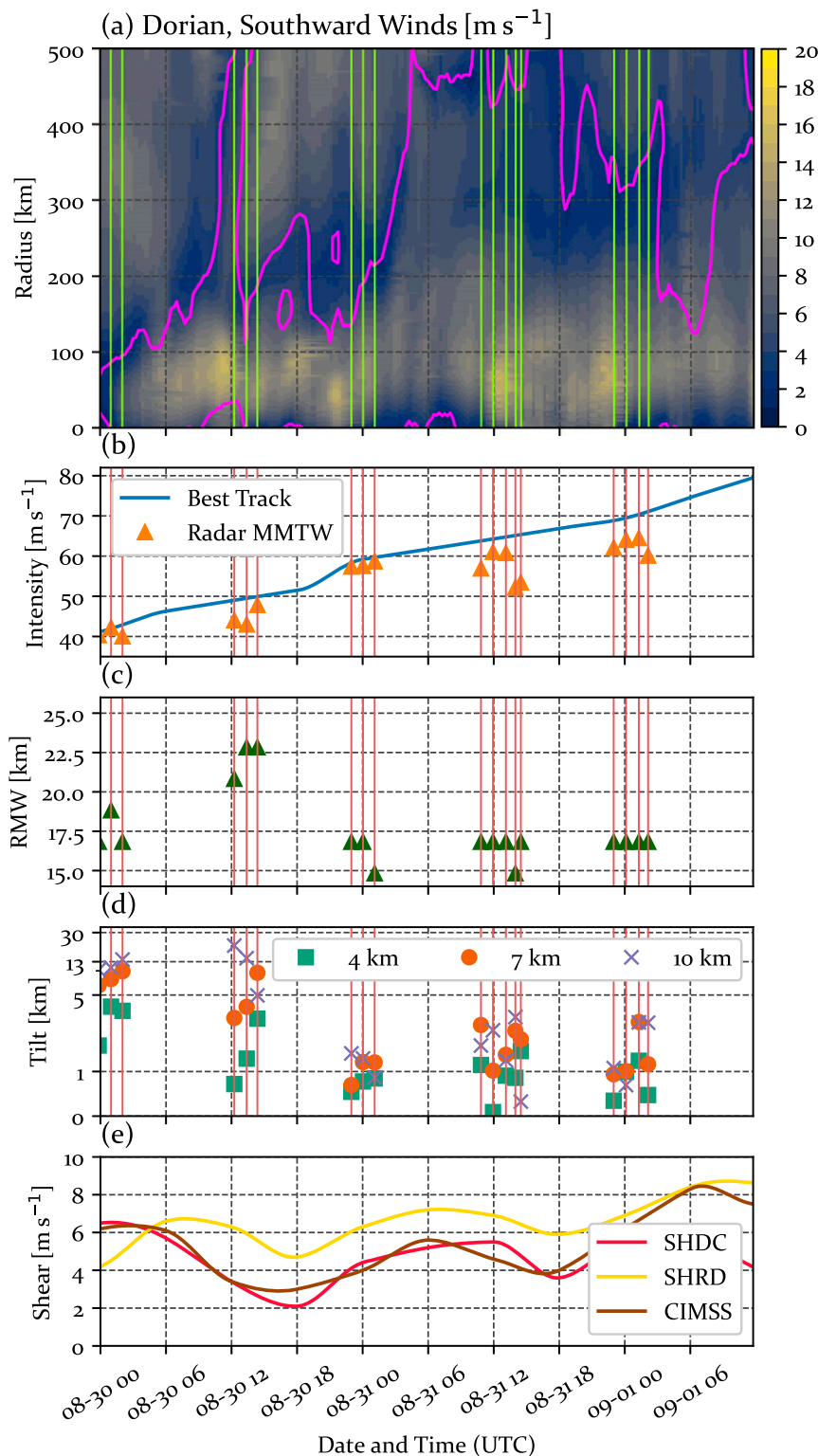


FIG. 8. (a) Hovmöller diagram of southward upper-level AMV-derived winds (shading) and radial wind zero line (magenta contour) smoothed with a 1-h running mean and averaged over a 45° wedge; (b) best track intensity and WP-3D radar-derived maximum mean tangential wind at 0.5-km height; (c) RMW at 0.5-km height; (d) 4.0-, 7.0-, and 10.0-km tilt magnitudes; and (e) operational shear calculations from SHDC, SHRD, and CIMSS. Vertical green and coral lines are the times of the flight swaths during the special observing period. In (d), y axis is semilogarithmic: linear from 0 to 2 and logarithmic thereafter.

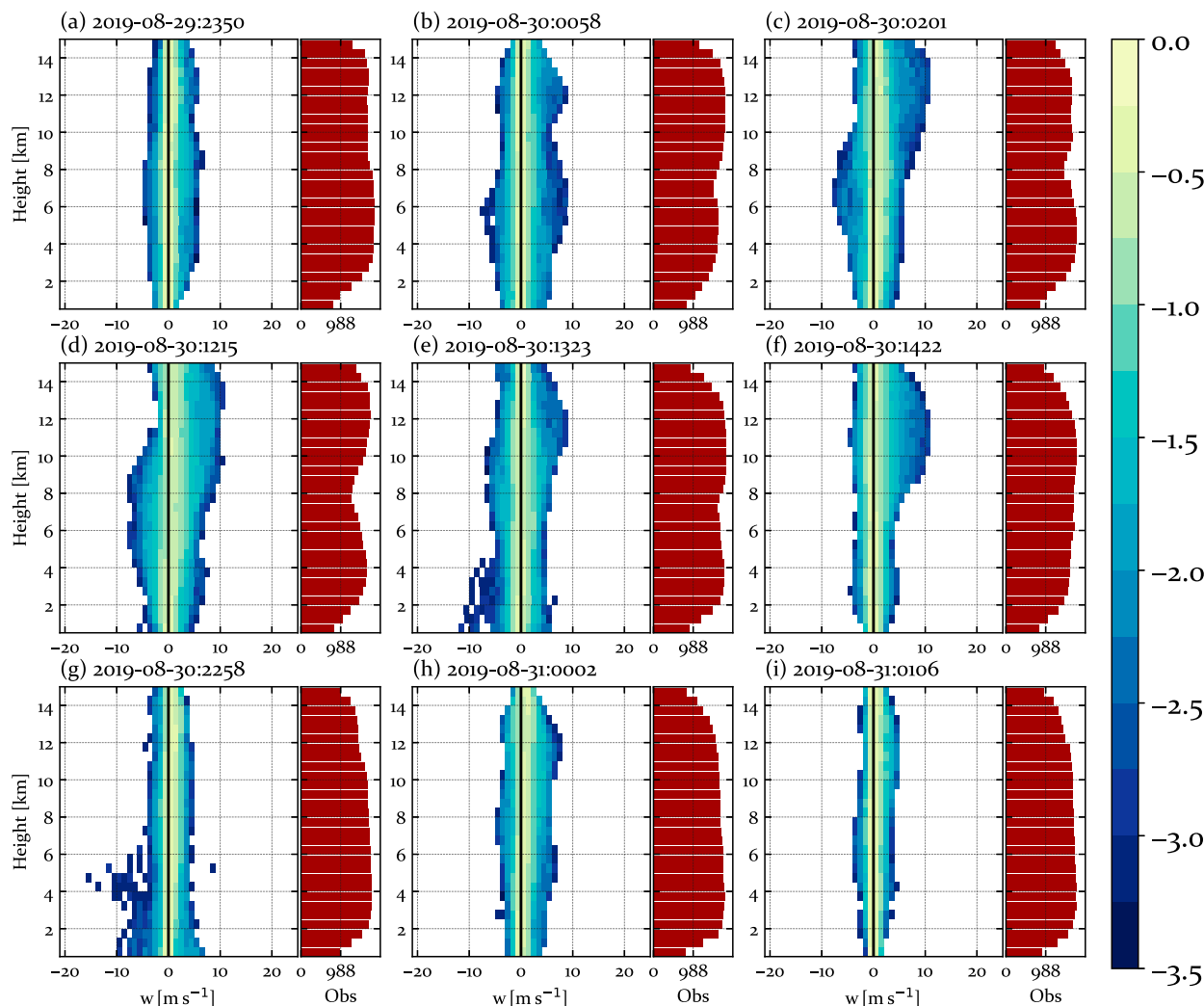


FIG. 9. For each of the flights in Fig. 7, (left) \log_{10} contour frequency by altitude diagrams of vertical winds (m s^{-1}) and (right) the total number of observations used at that given height at that time.

Using the AMV observations, we computed new vertical wind shear calculations which did not remove any component of the upper-layer flow unlike traditional shear methods. For the low-layer portion, we used both an AMV-derived layer flow for all winds below 650 hPa and the motion of the TC. By decomposing the flow in this way, we demonstrated that the cross-vortex upper-layer winds were near 7 m s^{-1} at the start of the special observing period window on 30 August, but the outflow reduced the upper-level cross-vortex flow to near zero during RI. Interestingly, while some of the new shear calculations showed shear reduction, they were not as drastic as shown in Part III. Operational shear calculations indicated shear values around 5 m s^{-1} , and the shear calculations developed herein indicated shear values either at or below the operational values.

b. Discussion

There are two important findings in this paper. First, to our knowledge, this is the first recorded observation of a vortex tilt

nutated analyzed directly using WP-3D aircraft radar. The flights into Dorian on 30 August captured three stages of tilt behavior in ARI: precession, nutation, and alignment. This evolution is concurrent with the observations of outflow surges at upper levels as shown by the AMVs, although aspects of this phenomenon have been noted in other studies (Black and Anthes 1971). While the previous papers in this series have either abstracted this behavior from satellite imagery (Part I, RHR) or used idealized models to simulate parts of it (Part II, Part III, RHR), this manuscript provides observational evidence of both important components of atypical RI: tilt nutations and outflow pushback. Using the filtering methods of Part I, we also demonstrated that the convective pulsing was approximately 6-hourly. This implies that the tilt nutation may also be approximately 6-hourly. This value falls within the 4–8-h range described in Part I. The WP-3D data captured the inward motion of the nutation with 3 observations over the span of 2 h.

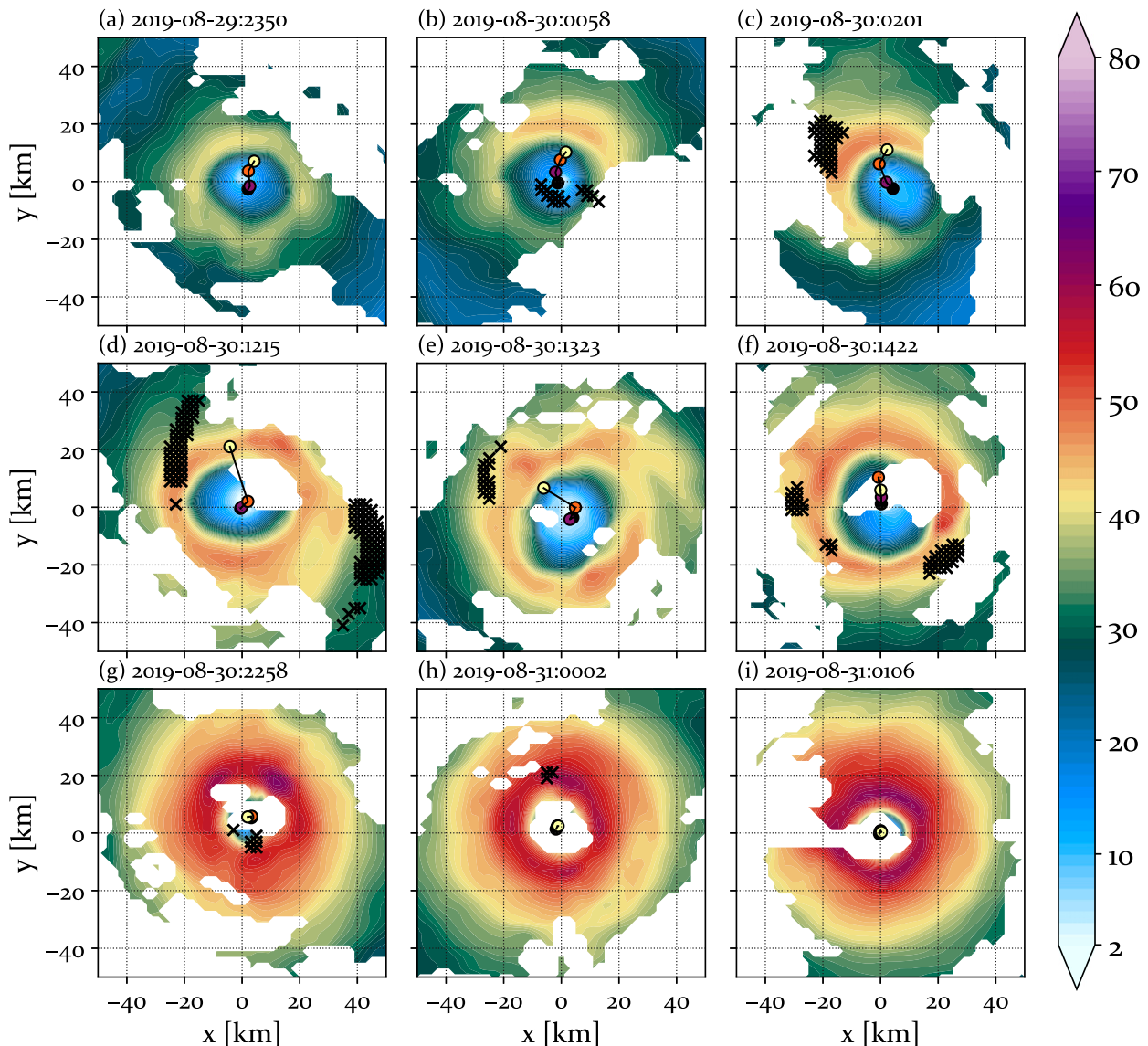


FIG. 10. The 2-km winds (m s^{-1}) for each of the flights from Fig. 9 with the 1–4- to 7–10-km tilt structure. Black \times symbols indicate columns that contain at least one observation of an updraft at least 7 m s^{-1} or greater.

Part of the underlying theme of all of the papers in this series is the inability of traditional shear calculations to capture the shear forcing on a TC adequately. Dorian's observations complicate this even further, since prior studies indicated that ARI was strictly a "moderate" shear phenomenon, where "moderate" is defined as 10 to 20 kt (or 5 to 10 m s^{-1}) of shear which was subsequently reduced by divergent outflow. Dorian's traditionally calculated shear values barely reached 5 m s^{-1} prior to its RI; however, perhaps more important than the actual shear value itself is whether or not the environmental flow is reaching the core and causing the TC to tilt. Based on the AMV analyses, the upper-layer flow came within 100 km of Dorian's core early on 30 August, and we know from the WP-3D observations that Dorian was tilting and wobbling

at this time. When isolating the two components used in shear calculations, the upper-level cross-vortex flow eventually reduced to 1 m s^{-1} and Dorian vertically aligned while the lower layers were between 2 and 6 m s^{-1} at this time. Based on this flow decomposition, the shear actually changes from "forward" shear to "reverse" shear, a condition in which the calculated environmental wind magnitudes are smaller at upper levels than they are at lower levels (Bond and Shapiro 1990; Terpstra et al. 2016). While outside the scope of this study, it would be worth investigating how TCs evolve when these conditions are met. Parts II and III demonstrated that the depth of the environmental flow can differentiate two traditionally analyzed shear values of 7.5 m s^{-1} ; the same may be true of forward and reverse shear orientation.

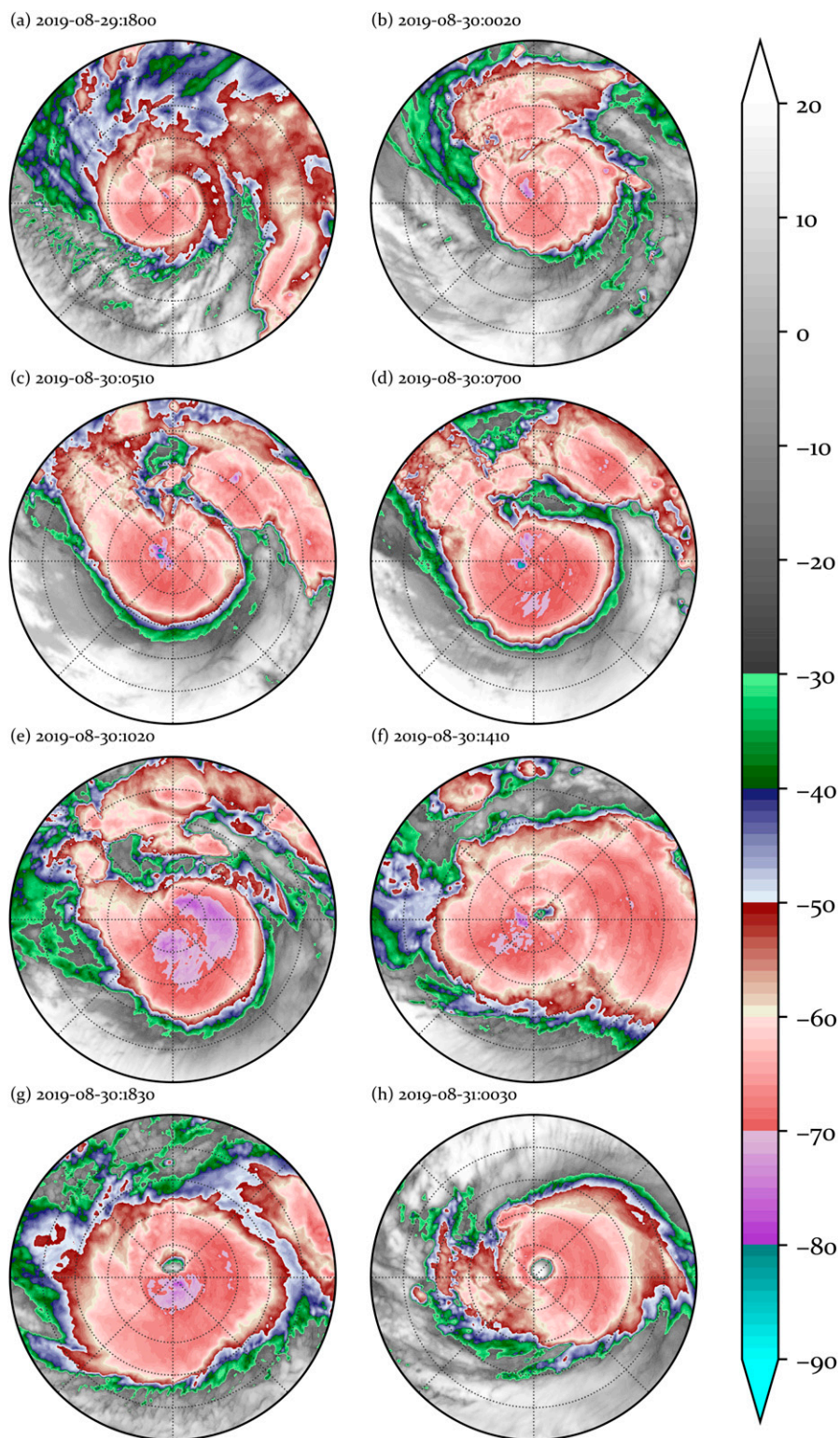


FIG. 11. Storm-relative IR brightness temperatures ($^{\circ}\text{C}$) of Dorian at (a) 1800 UTC 29 Aug; (b) 0020, (c) 0510, (d) 0700, (e) 1020, (f) 1410, and (g) 1830 UTC 30 Aug; and (h) 0030 UTC 31 Aug. Radial grid lines are every 50 km out to 250 km.

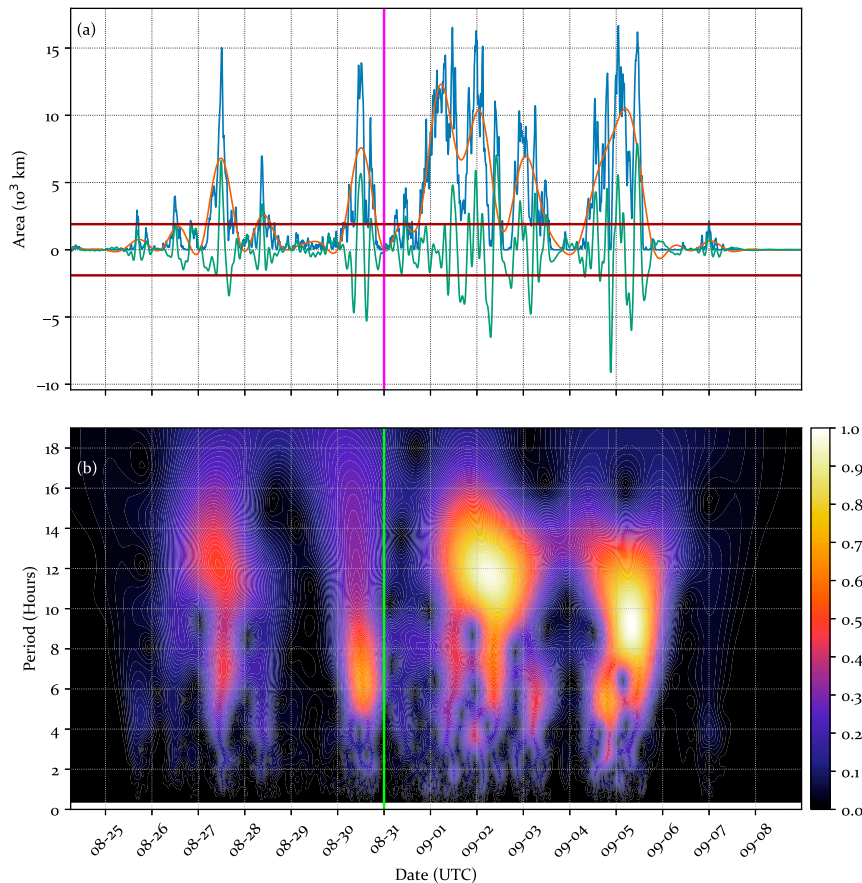


FIG. 12. (a) The area covered by IR brightness temperatures colder than -70°C within 200 km of Dorian during its evolution, its low-pass-filtered signal, and the bandpass-filtered signal. Dark red lines are ± 1 standard deviation of the bandpass signal. (b) Continuous wavelet transform normalized by maximum value (26.713 km^2). Time of distinct eye appearance is indicated by a magenta/green vertical line.

Up to this point, a climatological analysis of atypical RI has not been performed. Generally, it is easier to isolate this behavior in the northeastern Pacific basin using a simple analysis of, for example, the historical SHIPS database due to the climatological setup of the upper-level high pressure over Mexico (Part I). The Atlantic is significantly more complicated synoptically; however, three major TCs over the past few years (Joaquin in 2015, Matthew in 2016, and Dorian in 2019) have all exhibited ARI behavior. Dorian's evolution in apparent lower values of shear suggest that this behavior may be more common than previously thought. There exist a multitude of studies of TCs' interactions with upper-level troughs (e.g., Fischer et al. 2019; McTaggart-Cowan et al. 2013; Davis and Bosart 2003; Shi et al. 1997), but the interactions of TCs with upper-level ridges have largely been neglected outside of this series.

For operational applications of these principles, we must stress a specific point made in Part I and Part III: shear caused by an upper-level anticyclone or some other vertically shallow phenomenon can cause distinct behavioral uncertainties with TCs in this regime; therefore, we would recommend that until

an improved objective aid is provided, a careful examination of the upper-level wind fields is recommended to analyze the environment–TC interaction more completely. As has been demonstrated throughout this series, current numerical guidance struggles to capture the full ARI process. Future work will be devoted to developing objective forecast aids to improve understanding of TC–environment interactions as well as investigating more thoroughly why numerical models fail to capture ARI behavior. For example, we have experimented with new shear calculations that do not remove upper-level wind components, and this may be a worthwhile avenue for future research. Furthermore, a closer inspection of the SHIPS and SHIPS-RII parameters indicate that some of the newer thermodynamic predictors such as satellite measurements of total precipitable water upshear and the dry-air boundary layer flux predictor were not conducive to “classic” RI (Part I), and this relative dryness may have acted to suppress intensification in the numerical models. Finally, we still have yet to discuss the dynamics and thermodynamics at middle and lower levels as the shear is reduced and the precession and nutations damp, including some unique characteristics of a midlevel vortex that

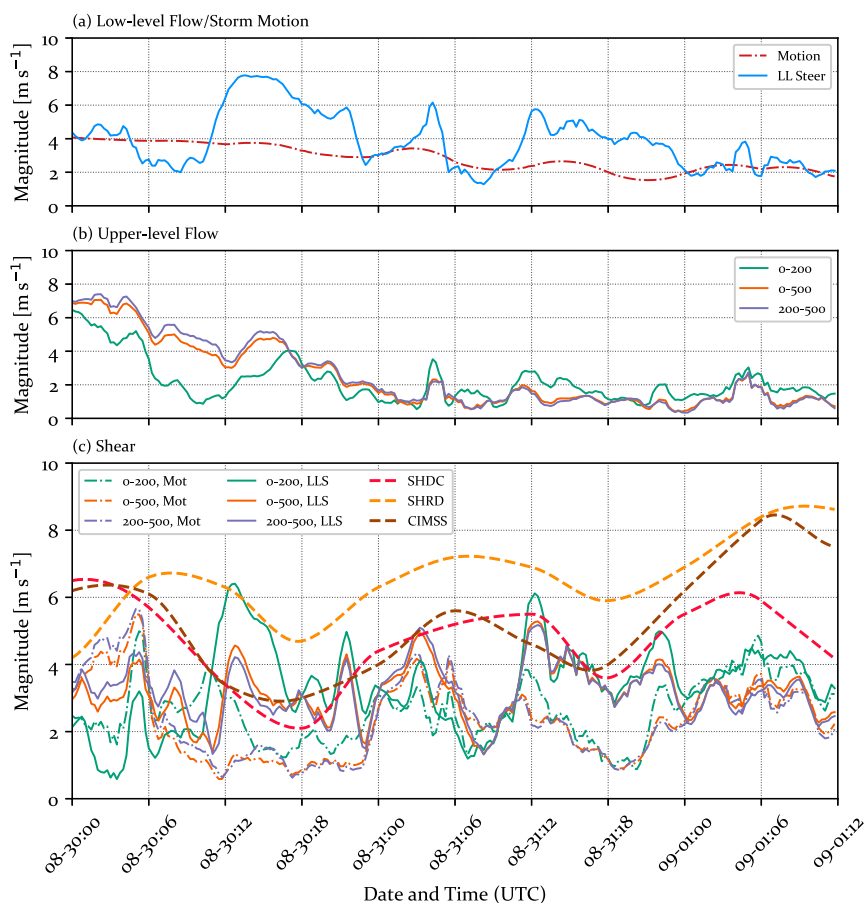


FIG. 13. (a) Low-level steering flow magnitude and storm motion magnitude. (b) Upper-level flow using various circles/annuli around the TC center. (c) Shear calculations using the various lower-level and upper-level quantities as well as the three operational shear calculations.

develops during atypical RI. Those discussions and analyses are reserved for future manuscripts.

Acknowledgments. DRR, CSV, and JDD all acknowledge funding from the ONR 6.1 TCRI DRI. The reprocessed AMV datasets were provided by Dave Stettner at UW-CIMSS. We are grateful to the flight crews and staff of NOAA's Aircraft Operations Center for flying the aircraft into Hurricane Dorian and to staff at AOML/HRD for retrievals, postprocessing, and archiving of the radar data. Graphics were produced using GrADS and matplotlib for Python—we thank the developers for their time and contributions. Analyses were performed using the Python packages numpy, scipy, pandas, and pyresample. We thank the authors of this software for their contributions. We also thank editor Kristen Corbosiero, Brian Tang, and two anonymous reviewers for their insightful comments that helped to improve this article's clarity and content.

Data availability statement. All data are publically available from their source institutions upon request.

APPENDIX A

Atmospheric Motion Vector Processing

The Advanced Baseline Imager (ABI) onboard the new-generation *GOES-16* is providing high-spatial- and high-temporal-resolution images that can be targeted on North Atlantic TCs. In addition to the routine full-disk scan every 10 min and continental United States (CONUS) scanning every 5 min, the ABI also has a flexible mesoscale scan mode for targeting limited domains in 1-min intervals. This “meso sector” is moveable and can be focused on a TC center with $10^\circ \times 10^\circ$ domain coverage that follows the storm motion with time. By using this 1-min ABI imagery, specially tailored automated algorithms have been developed to produce enhanced, high-resolution AMVs during a targeted TC event (Stettner et al. 2019). These spatially and temporally dense AMV datasets can provide critical dynamical information on the targeted storm and its near environment (Velden et al. 2017; Lewis et al. 2020).

As noted in the main article, for this study, AMV datasets were reprocessed by CIMSS from *GOES-16* ABI rapid scan

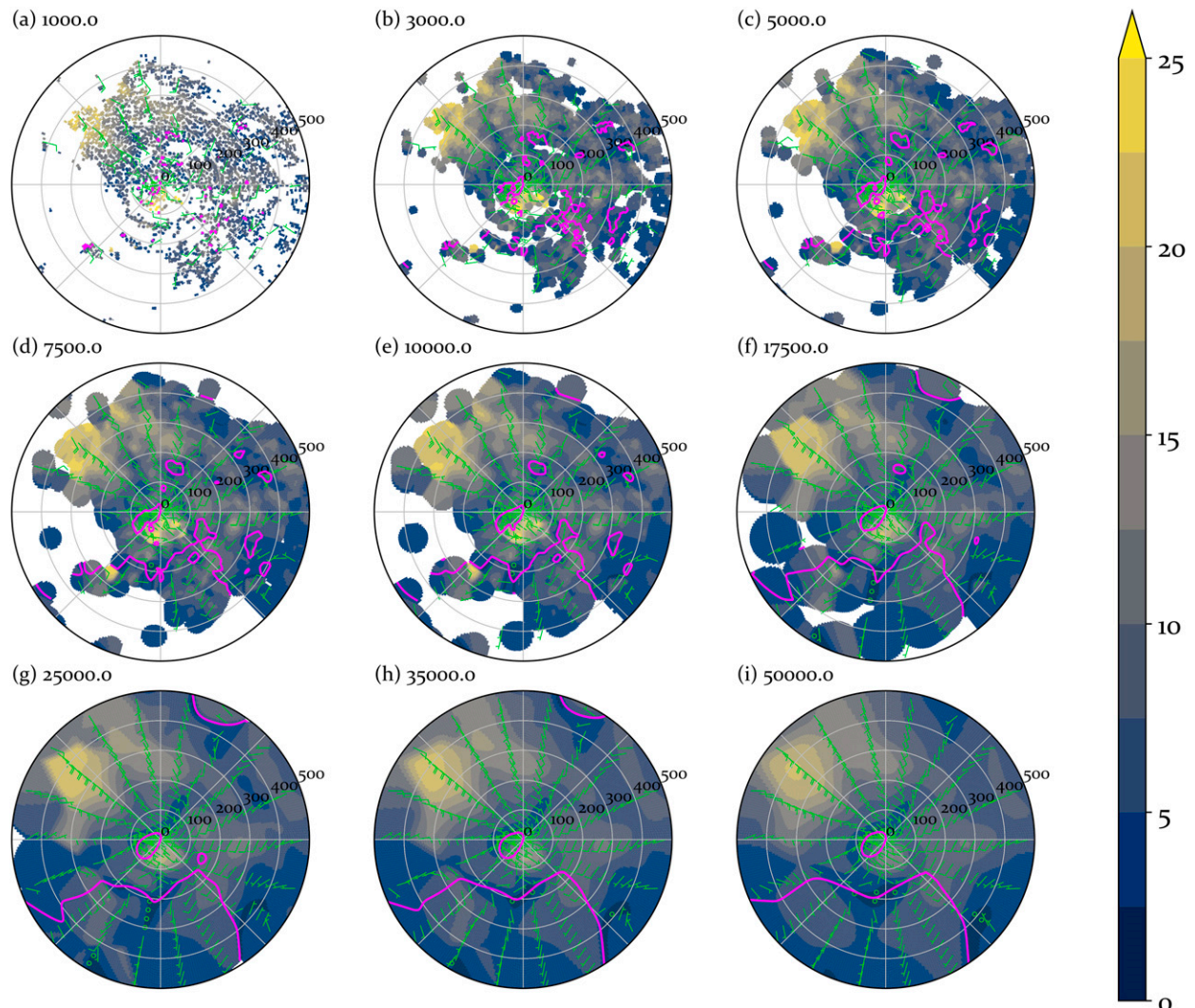


FIG. A1. Examples of the Gaussian resampling technique at 0700 UTC 30 Aug on the upper-layer winds (shading and green vectors; m s^{-1}) using different sigmas for the Gaussian, ranging from (a) 1 to (i) 50 km. Radial grid extends to 500 km. In (i) 50 km is used for subsequent analyses in the manuscript. Magenta contour is zero radial wind line.

imagery for the duration of Dorian when the meso sector was targeting the TC. Special processing strategies were imposed to enhance AMV coverage and maximize the information content to resolve the scales of the flow fields associated with the storm vortex and its near environment. Crucial to obtaining these observations is the continuous 1-min image sampling over targeted storms as mentioned above. In addition to using 1-min image triplets in the cloud tracking process, modifications for enhanced AMV coverage (vs routine full-disk processing) included increasing the target density, reducing the minimum gradient required for target identification, disabling stringent coherency requirements, and relaxing quality control (QC) constraints. Given the increased spatiotemporal resolution including good image navigation/coregistration, the reprocessed AMVs produced using the *GOES-16* meso-scans are considered to have accuracies superior to that of their conventional counterparts.

Further AMV processing details and examples can be found in [Stettner et al. \(2019\)](#).

A novel finding of [Part III](#) and [RHR](#) was that given the structure of the outflow of the TC and the distribution of AMVs at the top of the CDO, the outflow layer can be treated as a slab layer. The outflow upshear is generally confined to a 2-km layer beneath the tropopause. For the purposes of this manuscript, AMVs are grouped into three layers: surface to 650 hPa, 650 to 250 hPa, and then 250 hPa and higher. Given the relative dearth of AMV observations available in the middle layer in the tropics ([Sears and Velden 2012](#)), we focus on the upper and lower layers. This methodology is similar to the approach taken by [Velden and Sears \(2014\)](#) for the CIMSS shear calculation. These layers are designed to maximize the amount of data ingested for exploring relevant physical processes. The winds are corrected using the technique described by [Ahern and Cowan \(2018\)](#) to account for the curvature of

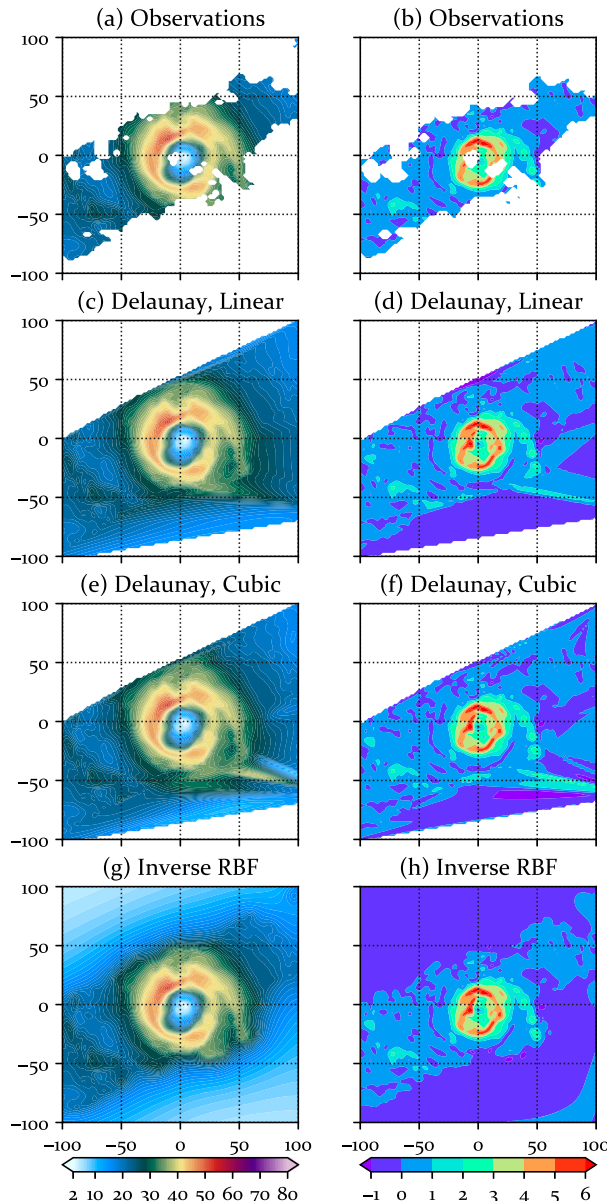


FIG. B1. Observations and interpolation examples of (left) winds (m s^{-1}) and (right) vorticity (10^{-3} s^{-1}) at 2.5-km height for the swath at 1323 UTC 30 Aug. Axis units are km.

Earth. Finally, they are resampled onto a cylindrical grid of 501 radial by 361 azimuthal points out to a radius of 500 km. For the resampling, Gaussian weighting is used. Figure A1 illustrates the upper-level wind field using a variety of sigma values from 1 km (Fig. A1a) to 50 km (Fig. A1i). Only observations within five sigma are used for an output grid point. While there are smaller-scale details associated with finer resampling values that may be of future interest to studies of outflow from convection (i.e., 5 km in Fig. A1c), we are more interested in the broad structure of the outflow for this particular study. For this reason, we use the 50-km sigma resampling output for all following analyses.

APPENDIX B

Center-Finding Ensemble

Before we attempt any center-finding, we employ three interpolation schemes in Cartesian space: linear Delaunay triangulation (Delaunay 1934), cubic Delaunay triangulation, and then inverse radial basis functions (RBFs). Interpolation examples for both the wind field and the vorticity field are shown in Fig. B1. Since we are limited to the wind and wind-derived fields, we then employ the use of two basic center-finding algorithms (Ryglicki and Hart 2015): the minimization of azimuthal variance of the wind using a brute force refinement methodology (MAVWBR) and then a straightforward vorticity centroid using a circle of 50-km (VYCR50). For MAVWBR, we use two annular widths: $4\sqrt{2}$ km and $10\sqrt{2}$ km. These are 2 and 5 times the grid spacing of the radar data with an added factor of $\sqrt{2}$ to account for diagonals across grid spaces. We first check each point in a 21×21 box around the domain center with 2-km spacing, picking the point where the maximum mean tangential wind (MMTW) is largest. We then take the new center and create a small nine by nine gridpoint box spanning $8 \text{ km} \times 8 \text{ km}$ (i.e., grid spacing of 1 km). We then refine again to spacings of 0.5 and 0.25 km before determining the center.

The sum total is nine possible centers for a given level: three center-finding methods applied to three different interpolation methods. We did try other center-finding algorithms, such as $6\sqrt{2}$ - and $8\sqrt{2}$ -km annular widths and vorticity centroids with weighting circles of 40 and 60 km, but they did not alter the analyses noticeably. We performed subjective spot checks in order to ensure and to confirm that the ensemble technique is valid, and so long as at least both sides of the RMW are sufficiently captured by the radar data, then the centers are reasonable.

REFERENCES

- Adams, J., and P. Swarztrauber, 1997: Spherpac 2.0: A model development facility. NCAR Tech. Note TN-436+STR, 62 pp., <https://doi.org/10.5065/D6Z899CF>.
- Ahern, K., and L. Cowan, 2018: Minimizing common errors when projecting geospatial data onto a vortex-centered space. *Geophys. Res. Lett.*, **45**, 12 032–12 039, <https://doi.org/10.1029/2018GL079953>.
- Avila, L. A., S. R. Stewart, R. Berg, and A. H. Hagen, 2020: Tropical cyclone report: Hurricane Dorian (24 August–7 September 2019). NHC Tech. Rep. AL052019, 74 pp., https://www.nhc.noaa.gov/data/tcr/AL052019_Dorian.pdf.
- Black, P. G., and R. A. Anthes, 1971: On the asymmetric structure of the tropical cyclone outflow layer. *J. Atmos. Sci.*, **28**, 1348–1366, [https://doi.org/10.1175/1520-0469\(1971\)028<1348:OTASOT>2.0.CO;2](https://doi.org/10.1175/1520-0469(1971)028<1348:OTASOT>2.0.CO;2).
- Bond, N. A., and M. A. Shapiro, 1990: Polar lows over the Gulf of Alaska in conditions of reverse shear. *Mon. Wea. Rev.*, **119**, 551–572, [https://doi.org/10.1175/1520-0493\(1991\)119<0551:PLOTGO>2.0.CO;2](https://doi.org/10.1175/1520-0493(1991)119<0551:PLOTGO>2.0.CO;2).
- Corbosiero, K. L., and J. Molinari, 2003: The relationship between storm motion, vertical wind shear, and convective asymmetries in tropical cyclones. *J. Atmos. Sci.*, **60**, 366–376, [https://doi.org/10.1175/1520-0469\(2003\)060<0366:TRBSMV>2.0.CO;2](https://doi.org/10.1175/1520-0469(2003)060<0366:TRBSMV>2.0.CO;2).

- Davis, C. A., and L. F. Bosart, 2003: Baroclinically induced tropical cyclogenesis. *Mon. Wea. Rev.*, **131**, 2730–2747, [https://doi.org/10.1175/1520-0493\(2003\)131<2730:BITC>2.0.CO;2](https://doi.org/10.1175/1520-0493(2003)131<2730:BITC>2.0.CO;2).
- Delaunay, B., 1934: Sur la sphère vide. *Bull. Acad. Sci. URSS, Cl. Sci. Math. Nat.*, **6**, 793–800.
- DeMaria, M., M. Mainelli, L. K. Shay, J. A. Knaff, and J. Kaplan, 2005: Further improvements to the Statistical Hurricane Intensity Prediction Scheme (SHIPS). *Wea. Forecasting*, **20**, 531–543, <https://doi.org/10.1175/WAF862.1>.
- Donion, J. P., C. D. Thorncroft, and C. S. Velden, 2014: The tropical cyclone diurnal cycle of mature hurricanes. *Mon. Wea. Rev.*, **142**, 3900–3919, <https://doi.org/10.1175/MWR-D-13-00191.1>.
- Finocchio, P. M., S. J. Majumdar, D. S. Nolan, and M. Iskandarani, 2016: Idealized tropical cyclone responses to the height and depth of environmental wind shear. *Mon. Wea. Rev.*, **144**, 2155–2175, <https://doi.org/10.1175/MWR-D-15-0320.1>.
- Fischer, M. S., B. H. Tang, and K. L. Corbosiero, 2019: A climatological analysis of tropical cyclone rapid intensification in environments of upper-tropospheric troughs. *Mon. Wea. Rev.*, **147**, 3693–3719, <https://doi.org/10.1175/MWR-D-19-0013.1>.
- Gamache, J. F., F. D. Marks, and F. Roux, 1994: Comparison of three airborne Doppler sampling techniques with airborne in situ wind observations in Hurricane Gustav (1990). *J. Atmos. Oceanic Technol.*, **12**, 171–181, [https://doi.org/10.1175/1520-0426\(1995\)012<0171:COTADS>2.0.CO;2](https://doi.org/10.1175/1520-0426(1995)012<0171:COTADS>2.0.CO;2).
- Guimond, S. R., G. M. Heymsfield, and F. J. Turk, 2010: Multiscale observations of Hurricane Dennis (2005): The effects of hot towers on rapid intensification. *J. Atmos. Sci.*, **67**, 633–654, <https://doi.org/10.1175/2009JAS3119.1>.
- , —, P. D. Reasor, and A. C. Didlake, 2016: The rapid intensification of Hurricane Karl (2010): New remote sensing observations of convective bursts from the Global Hawk platform. *J. Atmos. Sci.*, **73**, 3617–3639, <https://doi.org/10.1175/JAS-D-16-0026.1>.
- Hazelton, A. T., R. F. Rogers, and R. E. Hart, 2017a: Analyzing simulated convective bursts in two Atlantic hurricanes. Part I: Burst formation and development. *Mon. Wea. Rev.*, **145**, 3073–3094, <https://doi.org/10.1175/MWR-D-16-0267.1>.
- , R. E. Hart, and R. F. Rogers, 2017b: Analyzing simulated convective bursts in two Atlantic hurricanes. Part II: Intensity change due to bursts. *Mon. Wea. Rev.*, **145**, 3095–3117, <https://doi.org/10.1175/MWR-D-16-0268.1>.
- Jones, S. C., 1995: The evolution of vortices in vertical shear. Part I: Initially barotropic vortices. *Quart. J. Roy. Meteor. Soc.*, **121**, 821–851, <https://doi.org/10.1002/qj.49712152406>.
- Kaiser, J. F., and R. W. Schafer, 1980: On the use of the I_0 -sinh window for spectrum analysis. *IEEE Trans. Acoust. Speech Signal Process.*, **28**, 105–107, <https://doi.org/10.1109/TASSP.1980.1163349>.
- Kaplan, J., M. DeMaria, and J. A. Knaff, 2010: A revised tropical cyclone rapid intensification index for the Atlantic and eastern North Pacific basins. *Wea. Forecasting*, **25**, 220–241, <https://doi.org/10.1175/2009WAF2222280.1>.
- Knaff, J. A., S. P. Longmore, and D. A. Molenaar, 2014: An objective satellite-based tropical cyclone size climatology. *J. Climate*, **27**, 455–476, <https://doi.org/10.1175/JCLI-D-13-00096.1>.
- , C. R. Sampson, and K. D. Musgrave, 2018: An operational rapid intensification prediction aid for the western North Pacific. *Wea. Forecasting*, **33**, 799–811, <https://doi.org/10.1175/WAF-D-18-0012.1>.
- , —, and B. R. Strahl, 2020: A tropical cyclone rapid intensification prediction aid for the Joint Typhoon Warning Center's areas of responsibility. *Wea. Forecasting*, **35**, 1173–1185, <https://doi.org/10.1175/WAF-D-19-0228.1>.
- Kossin, J. P., 2002: Daily hurricane variability inferred from GOES infrared imagery. *Mon. Wea. Rev.*, **130**, 2260–2270, [https://doi.org/10.1175/1520-0493\(2002\)130<2260:DHVIFG>2.0.CO;2](https://doi.org/10.1175/1520-0493(2002)130<2260:DHVIFG>2.0.CO;2).
- Krishnamurti, T. N., S. Pattnaik, L. Stefanova, T. S. V. Vijaya Kumar, B. P. Mackey, A. J. O'Shay, and R. J. Pasch, 2005: The hurricane intensity issue. *Mon. Wea. Rev.*, **133**, 1886–1912, <https://doi.org/10.1175/MWR2954.1>.
- Landsea, C. W., and J. L. Franklin, 2013: Atlantic hurricane database uncertainty and presentation of a new database format. *Mon. Wea. Rev.*, **141**, 3576–3592, <https://doi.org/10.1175/MWR-D-12-00254.1>.
- Lewis, W., C. Velden, and D. Stettner, 2020: Strategies for assimilating high-density atmospheric motion vectors into a regional tropical cyclone forecast model (HWRf). *Atmosphere*, **11**, 673, <https://doi.org/10.3390/atmos11060673>.
- McTaggart-Cowan, R., T. J. Galarneau, L. F. Bosart, R. W. Moore, and O. Martius, 2013: A global climatology of baroclinically influenced tropical cyclogenesis. *Mon. Wea. Rev.*, **141**, 1963–1989, <https://doi.org/10.1175/MWR-D-12-00186.1>.
- Nuttall, A. H., 1981: Some windows with very good sidelobe behavior. *IEEE Trans. Acoust. Speech Signal Process.*, **29**, 84–91, <https://doi.org/10.1109/TASSP.1981.1163506>.
- Onderlinde, M. J., and D. Nolan, 2016: Tropical cyclone–relative environmental helicity and the pathways to intensification in shear. *J. Atmos. Sci.*, **73**, 869–890, <https://doi.org/10.1175/JAS-D-15-0261.1>.
- Reasor, P. D., and M. T. Montgomery, 2015: Evaluation of a heuristic model for tropical cyclone resilience. *J. Atmos. Sci.*, **72**, 1765–1782, <https://doi.org/10.1175/JAS-D-14-0318.1>.
- , —, and L. D. Grasso, 2004: A new look at the problem of tropical cyclones in vertical shear flow: Vortex resiliency. *J. Atmos. Sci.*, **61**, 3–22, [https://doi.org/10.1175/1520-0469\(2004\)061<0003:ANLATP>2.0.CO;2](https://doi.org/10.1175/1520-0469(2004)061<0003:ANLATP>2.0.CO;2).
- , R. F. Rogers, and S. Lorsolo, 2013: Environmental flow impacts on tropical cyclone structure diagnosed from airborne Doppler radar composites. *Mon. Wea. Rev.*, **141**, 2949–2969, <https://doi.org/10.1175/MWR-D-12-00334.1>.
- Riemer, M., and F. Laliberté, 2015: Secondary circulation of tropical cyclones in vertical wind shear: Lagrangian diagnostic and pathways of environmental interaction. *J. Atmos. Sci.*, **72**, 3517–3536, <https://doi.org/10.1175/JAS-D-14-0350.1>.
- Rogers, R., P. D. Reasor, and S. Lorsolo, 2013: Airborne Doppler observations of the inner-core structural differences between intensifying and steady-state tropical cyclone. *Mon. Wea. Rev.*, **141**, 2970–2991, <https://doi.org/10.1175/MWR-D-12-00357.1>.
- Rozoff, C. M., C. S. Velden, J. Kaplan, J. P. Kossin, and A. J. Wimmers, 2015: Improvements in the probabilistic prediction of tropical cyclone rapid intensification with passive microwave observations. *Wea. Forecasting*, **30**, 1016–1038, <https://doi.org/10.1175/WAF-D-14-00109.1>.
- Rygllicki, D. R., and R. E. Hart, 2015: An investigation of center-finding techniques for tropical cyclones in mesoscale models. *J. Appl. Meteor. Climatol.*, **54**, 825–846, <https://doi.org/10.1175/JAMC-D-14-0106.1>.
- , and D. Hodyss, 2016: A deeper analysis of center-finding techniques for tropical cyclones in mesoscale models. Part I: Low-wavenumber analysis. *J. Appl. Meteor. Climatol.*, **55**, 531–559, <https://doi.org/10.1175/JAMC-D-15-0125.1>.
- , J. D. Doyle, Y. Jin, D. Hodyss, and J. H. Cossuth, 2018a: The unexpected rapid intensification of tropical cyclones in

- moderate vertical wind shear. Part II: Vortex tilt. *Mon. Wea. Rev.*, **146**, 3801–3825, <https://doi.org/10.1175/MWR-D-18-0021.1>.
- , J. H. Cossuth, D. Hodyss, and J. D. Doyle, 2018b: The unexpected rapid intensification of tropical cyclones in moderate vertical wind shear. Part I: Overview and observations. *Mon. Wea. Rev.*, **146**, 3773–3800, <https://doi.org/10.1175/MWR-D-18-0020.1>.
- , J. D. Doyle, D. Hodyss, J. H. Cossuth, Y. Jin, K. C. Viner, and J. M. Schmidt, 2019: The unexpected rapid intensification of tropical cyclones in moderate vertical wind shear. Part III: Outflow–environment interaction. *Mon. Wea. Rev.*, **147**, 2919–2940, <https://doi.org/10.1175/MWR-D-18-0370.1>.
- , D. Hodyss, and G. Rainwater, 2020: The tropical cyclone as a divergent source in a background flow. *J. Atmos. Sci.*, **77**, 4189–4210, <https://doi.org/10.1175/JAS-D-20-0030.1>.
- Sampson, C. R., and A. J. Schrader, 2000: The Automated Tropical Cyclone Forecasting System (version 3.2). *Bull. Amer. Soc.*, **81**, 1231–1240, [https://doi.org/10.1175/1520-0477\(2000\)081<1231:TATCFS>2.3.CO;2](https://doi.org/10.1175/1520-0477(2000)081<1231:TATCFS>2.3.CO;2).
- , J. S. Goerss, J. A. Knaff, B. R. Strahl, E. M. Fukada, and E. A. Serra, 2018: Tropical cyclone gale wind radii estimates, forecasts, and error forecasts for the western North Pacific. *Wea. Forecasting*, **33**, 1081–1092, <https://doi.org/10.1175/WAF-D-17-0153.1>.
- Schecter, D. A., 2015: Response of a simulated hurricane to misalignment forcing compared to the predictions of a simple theory. *J. Atmos. Sci.*, **72**, 1235–1260, <https://doi.org/10.1175/JAS-D-14-0149.1>.
- Sears, J., and C. Velden, 2012: Validation of satellite-derived atmospheric motion vectors and analyses around tropical disturbances. *J. Appl. Meteor. Climatol.*, **51**, 1823–1834, <https://doi.org/10.1175/JAMC-D-12-024.1>.
- Shea, D. J., and W. M. Gray, 1973: The hurricane's inner core region. Part I: Symmetric and asymmetric structure. *J. Atmos. Sci.*, **30**, 1544–1564, [https://doi.org/10.1175/1520-0469\(1973\)030<1544:THICRI>2.0.CO;2](https://doi.org/10.1175/1520-0469(1973)030<1544:THICRI>2.0.CO;2).
- Shi, J. J., S. Chang, and S. Raman, 1997: Interaction between Hurricane Florence (1988) and an upper-tropospheric westerly trough. *J. Atmos. Sci.*, **54**, 1231–1247, [https://doi.org/10.1175/1520-0469\(1997\)054<1231:IBHFPA>2.0.CO;2](https://doi.org/10.1175/1520-0469(1997)054<1231:IBHFPA>2.0.CO;2).
- Smith, S. W., 2003: *Digital Signal Processing: A Practical Guide for Engineers and Scientists*. Elsevier, 650 pp.
- Steranka, J., E. B. Rodgers, and R. C. Gentry, 1986: The relationship between satellite measured convective bursts and tropical cyclone intensification. *Mon. Wea. Rev.*, **114**, 1539–1546, [https://doi.org/10.1175/1520-0493\(1986\)114<1539:TRBSMC>2.0.CO;2](https://doi.org/10.1175/1520-0493(1986)114<1539:TRBSMC>2.0.CO;2).
- Stettner, D., C. Velden, R. Rabin, S. Wanzong, J. Daniels, and W. Bresky, 2019: Development of enhanced vortex-scale atmospheric motion vectors for hurricane applications. *Remote Sens.*, **11**, 1981, <https://doi.org/10.3390/rs11171981>.
- Stevenson, S. N., K. L. Corborsiero, and J. Molinari, 2014: The convective evolution and rapid intensification of Hurricane Earl (2010). *Mon. Wea. Rev.*, **142**, 4364–4380, <https://doi.org/10.1175/MWR-D-14-00078.1>.
- Stewart, S. R., 2017: Tropical cyclone report: Hurricane Matthew (28 September–9 October 2016). NHC Tech. Rep. AL142016, 96 pp., https://www.nhc.noaa.gov/data/tcr/AL142016_Matthew.pdf.
- Terpstra, A., C. Michel, and T. Spengler, 2016: Forward and reverse shear environments during polar low genesis over the northeast Atlantic. *Mon. Wea. Rev.*, **144**, 1341–1354, <https://doi.org/10.1175/MWR-D-15-0314.1>.
- Velden, C. S., and J. Sears, 2014: Computing deep-tropospheric vertical wind shear analyses for tropical cyclone applications: Does the methodology matter? *Wea. Forecasting*, **29**, 1169–1180, <https://doi.org/10.1175/WAF-D-13-00147.1>.
- , W. Lewis, W. Bresky, D. Stettner, J. Daniels, and S. Wanzong, 2017: Assimilation of high-resolution satellite-derived atmospheric motion vectors: Impact on HWRF forecasts of tropical cyclone track and intensity. *Mon. Wea. Rev.*, **145**, 1107–1125, <https://doi.org/10.1175/MWR-D-16-0229.1>.
- Wadler, J. B., R. F. Rogers, and P. D. Reasor, 2018: The relationship between spatial variations in the structure of convective bursts and tropical cyclone intensification as determined by airborne Doppler radar. *Mon. Wea. Rev.*, **146**, 761–780, <https://doi.org/10.1175/MWR-D-17-0213.1>.
- Yuter, S. E., and R. A. Houze, 1995: Three-dimensional kinematic and microphysical evolution of Florida cumulonimbus. Part II: Frequency distributions of vertical velocity, reflectivity, and differential reflectivity. *Mon. Wea. Rev.*, **123**, 1941–1963, [https://doi.org/10.1175/1520-0493\(1995\)123<1941:TDKAME>2.0.CO;2](https://doi.org/10.1175/1520-0493(1995)123<1941:TDKAME>2.0.CO;2).
- Zawislak, J., H. Jiang, G. R. Alvey III, E. J. Zipser, R. F. Rogers, J. A. Zhang, and S. N. Stevenson, 2016: Observations of the structure and evolution of Hurricane Edouard (2014) during intensity change. Part I: Relationship between the thermodynamic structure and precipitation. *Mon. Wea. Rev.*, **144**, 3333–3354, <https://doi.org/10.1175/MWR-D-16-0018.1>.